

CRYSTAL IMAGE ANALYSIS USING 2D SYNCHROSQUEEZED TRANSFORMS

HAIZHAO YANG, JIANFENG LU, AND LEXING YING

ABSTRACT. We propose efficient algorithms based on a band-limited version of 2D synchrosqueezed transforms to extract mesoscopic and microscopic information from atomic crystal images. The methods analyze atomic crystal images as an assemblage of non-overlapping segments of 2D general intrinsic mode type functions, which are superpositions of non-linear wave-like components. In particular, crystal defects are interpreted as the irregularity of local energy; crystal rotations are described as the angle deviation of local wave vectors from their references; the gradient of a crystal elastic deformation can be obtained by a linear system generated by local wave vectors. Several numerical examples of synthetic and real crystal images are provided to illustrate the efficiency, robustness, and reliability of our methods.

1. INTRODUCTION

In materials science, crystal image analysis on a microscopic length scale has become an important research topic recently [4, 5, 12, 14, 24–27, 38]. The development of image acquisition techniques (such as high resolution transmission electron microscopy (HR-TEM) [18]) and the advancement of atomic simulation of molecular dynamics [1] or mean field models like phase field crystals [11, 13] create data of large scale crystalline solids with defects at an atomic resolution. This provides unprecedented opportunities in understanding materials properties at a microscopic level. Given that defects such as dislocations and grain boundaries are of crucial importance to materials properties, it is essential to have efficient tools to analyze large scale images and to extract information about defects in the system. Previously, this was done through analyzing the microscopic image manually; this is becoming impractical due to the extraordinarily large magnitude of the measurements and simulations we are dealing with nowadays, in particular, in the case of analyzing a time series of crystal images during an evolution process. Therefore, this calls for the development of efficient and automatic crystal image analysis tools.

In this work, we will limit our scope to 2D images of (slices of) polycrystalline materials and aim at extracting mesoscopic and microscopic information from the given images. This involves the identification of point defects, dislocations, deformations, grains and grain boundaries. Grains are material regions that are composed of a single crystal, possibly with different orientations (which will be referred as crystal rotations later, since we are working in 2D); they are usually slightly deformed due to defects and interactions with neighboring grains at grain boundaries. Grains might contain point defects like vacancies and interstitials, for which we would like identify their positions. Crystal analysis should also be able to locate cores and Burgers vectors for dislocations, which play an important role in crystal plasticity. We refer the readers to [19] for more background details of polycrystals and crystal defects. Our proposed method provides a reliable and efficient way for extracting this information from crystal images.

Date: September 18, 2015.

2000 Mathematics Subject Classification. 65T99, 74B20, 74E15, 74E25.

Key words and phrases. Crystal defect, elastic deformation, crystal rotation, 2D general wave shape, 2D general intrinsic mode type function, 2D band-limited synchrosqueezed transforms.

1.1. Our contribution. Due to the lattice structure on the microscopic scale, crystal images are highly oscillatory (see Figure 1 (right) as an example). Inspired by this, we introduce a new characterization of grains by studying 2D general shape functions and 2D general intrinsic mode type functions, which are superpositions of non-linear and non-stationary wave-like components (more precise definitions will be given in Section 2). Using these two concepts, a crystal image can be considered as an assemblage of 2D general intrinsic mode type functions with non-overlapping supports, specified propagating directions and smoothly varying local wave vectors (see Figure 1 (left) as an example). In this model, crystal defects and grain boundaries can be detected through the discontinuity and irregularity of these components; crystal rotations and crystal deformations are estimated from a linear system provided by local wave vectors of underlying wave-like components.

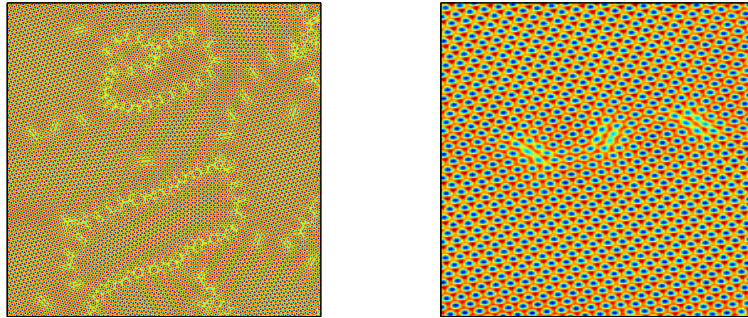


FIGURE 1. A phase field crystal (PFC) image and its zoomed-in image. Courtesy of Benedikt Wirth [14].

The study of superpositions of non-linear and non-stationary wave-like components has been an active line of analysis in the past two decades. The synchrosqueezing technique proposed in [10] is applied to analyze and decompose superpositions of 1D signals using the synchrosqueezed wavelet transform in [9]. Following the same methodology, synchrosqueezed wave packet transforms [35] and synchrosqueezed curvelet transforms [36] are proposed to analyze and decompose superpositions of 2D components. 2D synchrosqueezed transforms give a concentrated spectrum on the phase (spatial frequency) plane, which can help to obtain information like local wave vectors and a spectral density in the 4D phase space domain. Recent study on the robustness of these synchrosqueezed transforms in [32] supports their applications to real problems where noise is ubiquitous. These transforms have been applied to analyze seismic wave images with great success in [35, 36]. The numerical experiments in [34] show that these transforms have better statistical stability than the window Fourier transform in the application of canvas thread counting.

In this paper, we propose efficient algorithms to analyze crystal images by adapting 2D synchrosqueezed transforms to the problems at hand. First, 2D synchrosqueezed transforms are applied to obtain the synchrosqueezed energy distributions of underlying wave-like components. Second, since the synchrosqueezed energy is concentrating on local wave vectors, these local wave vectors can be estimated by averaging the supports of the synchrosqueezed energy distribution. Third, the irregularity of each wave-like component can be measured by the irregularity of its corresponding synchrosqueezed energy distribution. Finally, with such information ready, the crystal image can be analyzed as discussed previously.

1.2. Previous works. One important class of methods for crystal image analysis is variation based. General variational methods for texture classification and segmentation have been extensively studied (see [3, 8, 20, 23, 29, 30], for example).

The method in [4] proposed to segment crystal images into disjoint regions with different constant crystal rotations using the Chan-Vese level-set approximation in [8] of the piecewise constant Mumford-Shah segmentation in [21]. The method involves search for a global deformation $\phi : \Omega \rightarrow \mathbb{R}^2$ acting on all grains. To speed up the expensive optimization in [4], the authors in [5] proposed a convex relaxation via functional lifting and the authors in [25] proposed a more efficient version by penalizing the segmentation interfaces according to jumps in crystal rotations. Although a corresponding GPU implementation of these methods is very fast, a bottleneck still exists due to the large memory cost coming from the additional dimension for the functional lifting process.

More recently, Matt Elsey and Benedikt Wirth [12, 14] proposed a variational model based on finding a tensor map, the gradient of the inverse deformation $\nabla(\phi^{-1}) : \Omega \rightarrow \mathbb{R}^{2 \times 2}$ and developed an efficient $L^1 - L^2$ regularization scheme. Crystal defects, rotations, grain boundaries and strain can be recovered by the information hidden in $\nabla(\phi^{-1})$. In addition, a corresponding GPU implementation is proposed and it shortens the runtime for a 1024^2 image to about 40 seconds.

Another class of methods for texture classification and segmentation are based on a local, direction sensitive frequency analysis [24, 28]. [28] constructed an over-complete wavelet frame for texture feature extraction and segmented textures in a reduced feature space by clustering techniques. However, the frame is not sensitive to crystal rotations and local defects. Hence, it cannot distinguish two grains with a small angle boundary and cannot detect local defects. This method is neither capable of providing estimates of crystal deformations. The work [24] develops a heuristic method that uses a “wavelet like” patch according to a given reference crystal and quantify the similarity between local crystal patches with the reference. By looking up a prefabricated table of crystal rotation angles and their corresponding similarity, crystal rotations of each crystal patch can be estimated. However, in the case of deformed crystals, this method may be problematic.

The method to be presented in this paper follows a different spirit from those methods. It is based on a novel model characterizing deformed periodic textures using 2D general intrinsic mode type functions and an efficient phase space representation method, 2D synchrosqueezed transforms proposed recently. An analytic characterization of periodic textures allows rigorous analysis and indeed it is proved that 2D synchrosqueezed transforms can estimate the local wave vectors of underlying wave-like components of textures (grains in this paper) precisely under certain conditions. Most of all, non-linear deformations of crystals are available by solving a simple linear system provided by local wave vectors.

The rest of this paper is organized as follows. In Section 2, we introduce a crystal image model on the microscopic length scale based on 2D general intrinsic mode type functions and prove that 2D synchrosqueezed transforms are able to estimate the local properties of the underlying wave-like components of general intrinsic mode type functions. In Section 3, two efficient algorithms based on 2D discrete band-limited synchrosqueezed transforms are proposed to detect crystal defects, estimate crystal rotations and elastic deformations. In Section 4, several numerical examples of synthetic and real crystal images are provided to demonstrate the robustness and the reliability of our methods. Finally, we conclude with some discussion on future works in Section 5.

2. CRYSTAL IMAGE MODELS AND THEORY

In this section, at first, we describe a new model to characterize atomic crystal images. Inspired by the periodicity of crystal images, 2D general intrinsic mode type functions are defined as a key ingredient of the characterization of a perfect crystal image. Second, 2D synchrosqueezed transforms are briefly recalled to analyze underlying wave-like components in 2D general intrinsic mode type functions. We will prove that the 2D synchrosqueezed transforms accurately estimate the local wave vectors of these wave-like components, and hence provides a useful tool for crystal image analysis.

2.1. 2D general intrinsic mode type functions. A perfect crystal image, i.e., a single undeformed grain without defects, is characterized by a periodic function with two space variables. We will limit ourselves to simple crystals (Bravais lattices). In 2D space domain, there are five kinds of Bravais lattices: oblique, rectangular, centered rectangular (rhombic), hexagonal, and square [19]. The lattices and corresponding unit cells are shown in Figure 2. For each lattice type, through an affine transform, we can transform the

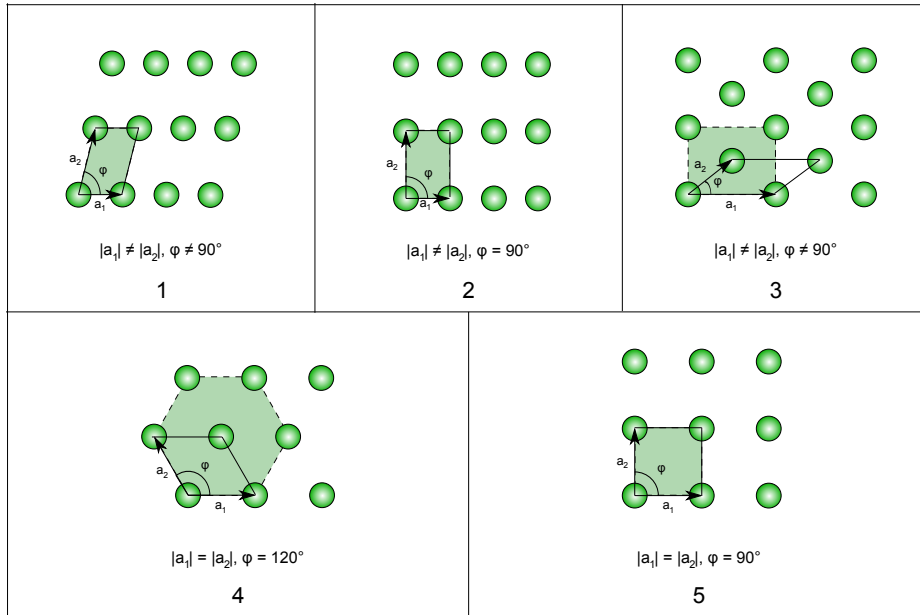


FIGURE 2. Five fundamental 2D Bravais lattices: 1 oblique, 2 rectangular, 3 centered rectangular (rhombic), 4 hexagonal, and 5 square. Courtesy of Wikipedia.

unit cell to a square. As an example, for the hexagonal lattice, the transform is given by

$$x \mapsto Fx; \quad F = \begin{pmatrix} 1 & -\frac{\sqrt{3}}{3} \\ 0 & \frac{2\sqrt{3}}{3} \end{pmatrix}.$$

Hence, by introducing the matrix F , we can set up a reference configuration function as

$$f(x) = \alpha S(2\pi Fx) + c,$$

for $x \in \mathbb{R}^2$. Here, $S(x)$ is a 2π periodic general shape function (the rigorous definition is given later), which has a unit $L^2([-\pi, \pi]^2)$ -norm and a zero mean. α and c are two parameters.

Allowing a rotation and a translation, a crystal image function for an undeformed grain is then modeled by

$$f(x) = \alpha S(2\pi NF(R_\theta x + z)) + c,$$

where N is the reciprocal of the lattice parameter, R_θ is the rotation matrix

$$R_\theta = \begin{pmatrix} \cos\theta & -\sin\theta \\ \sin\theta & \cos\theta \end{pmatrix}$$

corresponding to a rotation angle θ , and $z \in \mathbb{R}^2$ gives the translation. In the case of multi-grains, it is expected that

$$f(x) = \sum_{k=1}^M \chi_{\Omega_k}(x) (\alpha_k S_k(2\pi N_k F_k(R_{\theta_k} x + z_k)) + c_k),$$

where $\chi_{\Omega_k}(x)$ is the indicator function defined as

$$(1) \quad \chi_{\Omega_k}(x) = \begin{cases} 1, & x \in \Omega_k \\ 0, & \text{otherwise,} \end{cases}$$

and Ω_k is the domain of the k th grain with $\Omega_k \cap \Omega_j = \emptyset$, if $k \neq j$. With these notations, grain boundaries are interpreted as $\cup \partial \Omega_k$ (in real crystal images, grain boundaries would be a thin transition region instead of a sharp boundary $\cup \partial \Omega_k$). In the presence of local defects, e.g., an isolated defect and a terminating line of defects, $\cup \partial \Omega_k$ may include irregular boundaries and may contain point boundaries inside $\cup \Omega_k$.

Considering an uneven distribution of atoms on the mesoscopic length scale and possible reflection of light when generating crystal images, the amplitudes α_k and the global trends c_k are assumed to be smooth functions $\alpha_k(x)$ and $c_k(x)$, respectively, in the domain Ω_k .

Notice that the rotation matrix R_{θ_k} and the translation position z_k act as a linear transformation ψ_k from x to $\psi_k(x) = R_{-\theta_k}(x - z_k)$. In a more complicated case, a smooth non-linear deformation $\psi_k : \mathbb{R}^2 \rightarrow \mathbb{R}^2$ transferring an atom from position x to $\psi_k(x)$ is introduced. Let $\phi_k(x) = \psi_k^{-1}(x)$ defined in Ω_k , then the crystal image function becomes

$$(2) \quad f(x) = \sum_{k=1}^M \chi_{\Omega_k}(x) (\alpha_k(x) S_k(2\pi N_k F_k \phi_k(x)) + c_k(x)).$$

This motivates the definition of 2D general shape functions and 2D general intrinsic mode type functions as follows.

Definition 1 (2D general shape function). The 2D general shape function class S_M consists of periodic functions $S(x)$ with a periodicity $(2\pi, 2\pi)$, a unit $L^2([-\pi, \pi]^2)$ -norm, and an L^∞ -norm bounded by M satisfying the following conditions:

- (1) The 2D Fourier series of $S(x)$ is uniformly convergent;
- (2) $\sum_{n \in \mathbb{Z}^2} |\widehat{S}(n)| \leq M$ and $\widehat{S}(0, 0) = 0$;
- (3) Let Λ be the set of integers $\{|n_1| \in \mathbb{N} : \widehat{S}(n_1, n_2) \neq 0 \text{ or } \widehat{S}(n_2, n_1) \neq 0 \text{ for some } n_2 \in \mathbb{Z}\}$. The greatest common divisor of all the elements in Λ is 1.

The requirement that $\widehat{S}(0, 0) = 0$, which is equivalent to a zero mean over $[-\pi, \pi]^2$, guarantees a well-separation between the oscillatory part $\alpha_k(x) S_k(2\pi N_k F_k \phi_k(x))$ and the smooth trend $c_k(x)$ in (2), when N_k is sufficiently large. The third condition implies the uniqueness of similar oscillatory patterns in S_M up to a scaling, i.e., if $S(x) \in S_M$, $S(Nx) \notin S_M$ for any positive integer $N > 1$.

Definition 2 (2D general intrinsic mode type function (GIMT)). A function $f(x) = \alpha(x)s(2\pi NF\phi(x))$ is a 2D GIMT of type (M, N, F) , if $S(x) \in S_M$, $\alpha(x)$ and $\phi(x)$ satisfy the conditions below.

$$\begin{aligned} \alpha(x) &\in C^\infty, \quad |\nabla \alpha| \leq M, \quad 1/M \leq \alpha \leq M, \\ \phi(x) &\in C^\infty, \quad 1/M \leq |\nabla(n^T F\phi)/|n^T F|| \leq M, \quad \text{and} \\ |\nabla^2(n^T F\phi)/|n^T F|| &\leq M, \quad \forall n \in \mathbb{Z}^2 \quad \text{s.t. } \widehat{S}(n) \neq 0. \end{aligned}$$

Hence, in the domain Ω_k of each grain, the crystal image is a superposition of a 2D general intrinsic mode type function and a smooth trend. Applying the 2D Fourier series of each 2D general shape function $S_k(x)$, it holds that

$$\begin{aligned} f(x) &= \sum_{k=1}^M \chi_{\Omega_k}(x) (\alpha_k(x) S_k(2\pi N_k F_k \phi_k(x)) + c_k(x)) \\ (3) \quad &= \sum_{k=1}^M \chi_{\Omega_k}(x) \left(\sum_{n \in \mathbb{Z}^2} \alpha_k(x) \widehat{S}_k(n) e^{2\pi i N_k n^T F_k \phi_k(x)} + c_k(x) \right), \end{aligned}$$

In the domain Ω_k , each underlying wave-like component

$$\alpha_k(x) \widehat{S}_k(n) e^{2\pi i N_k n^T F_k \phi_k(x)}$$

is an intrinsic mode type function studied in [35, 36]. Hence, if they satisfy the well-separation condition defined in [35, 36] and each N_k is large enough, the 2D synchrosqueezed wave packet transforms and the synchrosqueezed curvelet transforms are expected to estimate the local wave vectors $N_k \nabla(n^T F_k \phi_k(x))$ accurately for x away from $\partial\Omega_k$.

Based on the estimates of local wave vectors, it is possible to define and analyze crystal rotations as follows.

Definition 3. Given a reference configuration $s(2\pi NFx)$, a deformation $\phi(x)$, an amplitude function $\alpha(x)$ and a trend function $c(x)$ such that $f(x) = \alpha(x)s(2\pi NF\phi(x)) + c(x)$ is a 2D GIMT of type (M, N, F) , suppose $\widehat{S}(n) \neq 0$, then the reference configuration has a local wave vector $v(n) = Nn^T F$ and $f(x)$ has a local wave vector $v_\phi = Nn^T F\nabla\phi(x)$. The local rotation function of $f(x)$ with respect to $v(n)$ is defined as

$$\beta(f)(x) = \arg(v_\phi(x)) - \arg(v(n)),$$

where $\arg(\nu)$ means the argument of a vector ν .

In the case of an undeformed crystal image $f(x) = \alpha(x)s(2\pi NF(R_\theta x + z)) + c(x)$, $\phi(x) = R_\theta x + z$ is a composition of a rotation and a translation. Then the local rotation function $\beta(f)(x) = \theta$ with respect to any local wave vector $v(n)$. This agrees with an intuition of a global crystal rotation. However, a global crystal rotation is not well defined in a real crystal image due to a non-linear crystal deformation. This motivates the definition of a local crystal rotation in Definition 3. Because the non-linear deformation $\phi(x)$ is a smooth function with $\det(\nabla\phi(x)) \approx 1$, local rotation functions $\beta(f)(x)$ vary smoothly and are approximately the same with respect to any local wave vector.

2.2. 2D synchrosqueezed transforms. For the sake of convenience, we adopt the name 2D synchrosqueezed transforms instead of specifying 2D synchrosqueezed wave packet transform or 2D synchrosqueezed curvelet transforms. Actually, when the scaling parameters s and t in the 2D synchrosqueezed curvelet transforms are equal, these transforms become 2D synchrosqueezed wave packet transforms. For the same reason, we prefer a uniform name general wave packet transforms, instead of the wave packet transforms in [35] and the general curvelet transforms in [36]. Before a brief review of these transforms, here are some notations.

(1) The scaling matrix

$$A_a = \begin{pmatrix} a^t & 0 \\ 0 & a^s \end{pmatrix},$$

where a is the distance from the center of one general wave packet to the origin in the Fourier domain.

(2) A unit vector $e_\theta = (\cos\theta, \sin\theta)^T$ with a rotation angle θ .

(3) θ_α represents the argument of a given vector α .

(4) $w(x)$ of $x \in \mathbb{R}^2$ denotes a mother wave packet, which is in the Schwartz class and has a non-negative, radial, real-valued, smooth Fourier transform $\widehat{w}(\xi)$ with a support equal to a ball $B_d(0)$ centered at the origin with a radius $d \leq 1$ in the Fourier domain. The mother wave packet is required to obey the admissibility condition: $\exists 0 < c_1 < c_2 < \infty$ such that

$$c_1 \leq \int_0^{2\pi} \int_1^\infty a^{-(t+s)} |\widehat{w}(A_a^{-1} R_\theta^{-1}(\xi - a \cdot e_\theta))|^2 a da d\theta \leq c_2$$

for any $|\xi| \geq 1$.

With the notations above, it is ready to define a family of general wave packets through scaling, modulation, and translation as follows, controlled by geometric parameters s and t .

Definition 4. For $\frac{1}{2} < s \leq t < 1$, define $\widehat{w_{a\theta b}}(\xi) = \widehat{w}(A_a^{-1} R_\theta^{-1}(\xi - a \cdot e_\theta)) e^{-2\pi i b \cdot \xi} a^{-\frac{t+s}{2}}$ as a general wave packet in the Fourier domain. Equivalently, in the space domain, the corresponding general wave packet is

$$\begin{aligned} w_{a\theta b}(x) &= \int_{\mathbb{R}^2} \widehat{w}(A_a^{-1} R_\theta^{-1}(\xi - a \cdot e_\theta)) e^{-2\pi i b \cdot \xi} e^{2\pi i \xi \cdot x} a^{-\frac{t+s}{2}} d\xi \\ &= a^{\frac{t+s}{2}} \int_{\mathbb{R}^2} \widehat{w}(y) e^{-2\pi i b \cdot (R_\theta A_a y + a \cdot e_\theta)} e^{2\pi i x \cdot (R_\theta A_a y + a \cdot e_\theta)} dy \\ &= a^{\frac{t+s}{2}} e^{2\pi i a(x-b) \cdot e_\theta} w(A_a R_\theta^{-1}(x-b)). \end{aligned}$$

In such a way, a family of general wave packets $\{w_{a\theta b}(x), a \in [1, \infty), \theta \in [0, 2\pi), b \in \mathbb{R}^2\}$ is constructed.

Similar to classical time-frequency transforms, the general wave packet transform is defined to be the inner product of a given signal and each general wave packet as follows.

Definition 5. The general wave packet transform of a function $f(x)$ is a function

$$\begin{aligned} W_f(a, \theta, b) &= \langle w_{a\theta b}, f \rangle = \int_{\mathbb{R}^2} \overline{w_{a\theta b}(x)} f(x) dx \\ &= \langle \widehat{w_{a\theta b}}, \widehat{f} \rangle = \int_{\mathbb{R}^2} \overline{\widehat{w_{a\theta b}}(\xi)} \widehat{f}(\xi) d\xi \end{aligned}$$

for $a \in [1, \infty)$, $\theta \in [0, 2\pi)$, $b \in \mathbb{R}^2$.

Definition 6. The local wave-vector estimation of a function $f(x)$ at (a, θ, b) is

$$(4) \quad v_f(a, \theta, b) = \frac{\nabla_b W_f(a, \theta, b)}{2\pi i W_f(a, \theta, b)}$$

for $a \in [1, \infty)$, $\theta \in [0, 2\pi)$, $b \in \mathbb{R}^2$ such that $W_f(a, \theta, b) \neq 0$.

In [35, 36], it has been proved that $v_f(a, \theta, b)$ accurately estimates local wave-vectors independently of the amplitude functions α_k or the position b from a finite superposition of wave-like components without boundaries. Hence, if the coefficients with the same v_f are reallocated together, then the nonzero energy would be concentrating around local wave-vectors of $f(x)$. Mathematically speaking, the synchrosqueezed energy distribution is defined as follows.

Definition 7. Given $f(x)$, $W_f(a, \theta, b)$, and $v_f(a, \theta, b)$, the synchrosqueezed energy distribution $T_f(v, b)$ is

$$(5) \quad T_f(v, b) = \int |W_f(a, \theta, b)|^2 \delta(\Re v_f(a, \theta, b) - v) a da d\theta$$

for $v \in \mathbb{R}^2$, $b \in \mathbb{R}^2$.

If the Fourier transform $\hat{f}(\xi)$ vanishes for $|\xi| < 1$, one can check the following L^2 -norms equivalence up to a uniform constant factor following the proof of [7, Theorem 1], i.e.,

$$(6) \quad \int |W_f(a, \theta, b)|^2 a da d\theta db = \Theta \left(\int |f(x)|^2 dx \right).$$

Our goal is to apply and adapt the 2D synchrosqueezed transforms to analyze the 2D general intrinsic mode type functions in the image function (3). This problem is similar to but different from the 1D general mode decomposition problems studied in [31, 33], where 1D synchrosqueezed transforms are applied to estimate the instantaneous properties of 1D general intrinsic mode type functions. Generalizing the conclusions in [33, 36], the theorem below shows that the 2D synchrosqueezed transforms precisely estimate the local wave vectors of the wave-like components in (3) at the points away from boundaries.

Theorem 8. For a 2D general intrinsic mode type function $f(x)$ of type (M, N, F) with $|F| \geq 1$, any $\epsilon > 0$ and any $r > 1$, we define

$$R_\epsilon = \left\{ (a, \theta, b) : |W_f(a, \theta, b)| \geq a^{-\frac{s+t}{2}} \sqrt{\epsilon}, \quad a \leq 2MNr \right\}$$

and

$$Z_n = \left\{ (a, \theta, b) : \left| A_a^{-1} R_\theta^{-1} (a \cdot e_\theta - N \nabla(n^T F \phi(b))) \right| \leq d, \quad a \leq 2MNr \right\}$$

For fixed M , r , s , t , d , and ϵ , there exists $N_0(M, r, s, t, d, \epsilon) > 0$ such that for any $N > N_0(M, r, s, t, d, \epsilon)$ and a 2D GIMT $f(x)$ of type (M, N, F) , the following statements hold.

(i) $\{Z_n : \hat{S}(n) \neq 0\}$ are disjoint and $R_\epsilon \subset \bigcup_{\hat{S}(n) \neq 0} Z_n$;

(ii) For any $(a, \theta, b) \in R_\epsilon \cap Z_n$,

$$\frac{|v_f(a, \theta, b) - N \nabla(n^T F \phi(b))|}{|N \nabla(n^T F \phi(b))|} \lesssim \sqrt{\epsilon}.$$

For simplicity, the notations $\mathcal{O}(\cdot)$, \lesssim and \gtrsim are used when the implicit constants may only depend on M , s , t , d and K . The proof of the theorem is similar to those theorems in [33, 36] and relies on two lemmas in [36]. Although the parameter d is set to be 1 in [36], it is easy to extend these two lemmas for a general value of d . We state the generalizations here, leaving the proofs to the reader.

Lemma 1. Suppose $f(x) = \sum_{k=1}^K f_k(x) = \sum_{k=1}^K e^{-(\phi_k(x) - c_k)^2 / \sigma_k^2} \alpha_k(x) e^{2\pi i N \phi_k(x)}$ is a well-separated superposition of type (M, N, K) (refer to [36]). Set

$$\Omega = \left\{ (a, \theta) : a \in \left(\frac{N}{2M}, 2MN \right), \exists k \text{ s.t. } |\theta_{\nabla \phi_k(b)} - \theta| < \theta_0 \right\},$$

where $\theta_0 = \arcsin((\frac{M}{N})^{t-s})$. For any $\epsilon > 0$, there exists $N_0(M, s, t, d, \epsilon)$ such that the following estimation of $W_f(a, \theta, b)$ holds for any $N > N_0$.

(1) If $(a, \theta) \in \Omega$,

$$W_f(a, \theta, b) = a^{-\frac{s+t}{2}} \left(\sum_{k: |\theta_{\nabla \phi_k(b)} - \theta| < \theta_0} f_k(b) \hat{w} \left(A_a^{-1} R_\theta^{-1} (a \cdot e_\theta - N \nabla \phi_k(b)) \right) + \mathcal{O}(\epsilon) \right);$$

(2) Otherwise,

$$W_f(a, \theta, b) = a^{-\frac{s+t}{2}} \mathcal{O}(\epsilon).$$

Lemma 2. Suppose $f(x) = \sum_{k=1}^K f_k(x) = \sum_{k=1}^K e^{-(\phi_k(x)-c_k)^2/\sigma_k^2} \alpha_k(x) e^{2\pi i N \phi_k(x)}$ is a well-separated superposition of type (M, N, K) . For any $\epsilon > 0$, there exists $N_0(M, s, t, d, \epsilon)$ such that the following estimation of $\nabla_b W_f(a, \theta, b)$ holds for any $N > N_0$.

$$\nabla_b W_f(a, \theta, b) = a^{-\frac{s+t}{2}} \left(2\pi i N \sum_{k: |\theta_{\nabla\phi_k(b)} - \theta| < \theta_0} \nabla\phi_k(b) f_k(b) \hat{w}(A_a^{-1} R_\theta^{-1}(a \cdot e_\theta - N \nabla\phi(b))) + \mathcal{O}(\epsilon) \right),$$

when

$$(a, \theta) \in \Omega = \left\{ (a, \theta) : a \in \left(\frac{N}{2M}, 2MN \right), \exists k \text{ s.t. } |\theta_{\nabla\phi_k(b)} - \theta| < \theta_0 \right\}.$$

In the scope of this paper, we have $\sigma_k = \infty$ for all k . Now, we are ready to prove Theorem 8.

Proof of Theorem 8. By the uniform convergence of the 2D Fourier series of general shape functions, we have

$$W_f(a, \theta, b) = \sum_{n \in \mathbb{Z}^2} W_{f_n}(a, \theta, b),$$

where $f_n(x) = \widehat{S}(n) \alpha(x) e^{2\pi i N n^T F \phi(x)}$. Introduce the short hand notation, $\tilde{\phi}_n(x) = n^T F \phi(x) / |n^T F|$, then

$$f_n(x) = \widehat{S}(n) \alpha(x) e^{2\pi i N |n^T F| \tilde{\phi}_n(x)}.$$

By the property of 2D general intrinsic mode functions, $f_n(x)$ is a well-separated superposition of type $(M, N|n^T F|, 1)$ defined in [36].

For each n , we estimate $W_{f_n}(a, \theta, b)$. By Lemma 1, there exists a uniform $N_1(M, s, t, d, \epsilon)$ independent of n such that, if $N|n^T F| > N_1$,

$$W_{f_n}(a, \theta, b) = a^{-\frac{s+t}{2}} (f_n(b) \hat{w}(A_a^{-1} R_\theta^{-1}(a \cdot e_\theta - N|n^T F| \nabla \tilde{\phi}_n(b))) + |\widehat{S}(n)| \mathcal{O}(\epsilon))$$

for $(a, \theta) \in \Omega_n$, and

$$W_{f_n}(a, \theta, b) = a^{-\frac{s+t}{2}} |\widehat{S}(n)| \mathcal{O}(\epsilon)$$

for $(a, \theta) \notin \Omega_n$. Here

$$\Omega_n = \left\{ (a, \theta) : a \in \left(\frac{N|n^T F|}{2M}, 2MN|n^T F| \right), |\theta_{\nabla\tilde{\phi}_n(b)} - \theta| < \theta_0 \right\},$$

and $\theta_0 = \arcsin((\frac{M}{N|n^T F|})^{t-s})$. Let $\Gamma_{a\theta} = \{n \in \mathbb{Z}^2 : (a, \theta) \in \Omega_n\}$, then

$$\begin{aligned} W_f(a, \theta, b) &= a^{-\frac{s+t}{2}} \left(\sum_{n \in \Gamma_{a\theta}} f_n(b) \hat{w}(A_a^{-1} R_\theta^{-1}(a \cdot e_\theta - N|n^T F| \nabla \tilde{\phi}_n(b))) + \sum_n |\widehat{S}(n)| \mathcal{O}(\epsilon) \right) \\ &= a^{-\frac{s+t}{2}} \left(\sum_{n \in \Gamma_{a\theta}} f_n(b) \hat{w}(A_a^{-1} R_\theta^{-1}(a \cdot e_\theta - N|n^T F| \nabla \tilde{\phi}_n(b))) + \mathcal{O}(\epsilon) \right). \end{aligned}$$

Notice that for any $n \neq \tilde{n}$, the distance between the local wave vectors $N|n^T F| \nabla \tilde{\phi}_n(b)$ and $N|\tilde{n}^T F| \nabla \tilde{\phi}_{\tilde{n}}(b)$ are bounded below. In fact,

$$\begin{aligned} |N|n^T F| \nabla \tilde{\phi}_n(b) - N|\tilde{n}^T F| \nabla \tilde{\phi}_{\tilde{n}}(b)| &= N|(n - \tilde{n})^T F \nabla \phi(b)| \\ &\geq \frac{N}{M}|(n - \tilde{n})^T F| \geq \frac{N}{M}. \end{aligned}$$

The first inequality above is due to the definition of 2D general intrinsic mode type function. Observe that the support of a general wave packet centered at $(a \cos(\theta), a \sin(\theta))$ is within a disk with a radius of length da^t . Because the range of a of interest is $a \leq 2MNr$, the general wave packets of interest have supports of

size at most $2d(2MNr)^t$. Hence, if $\frac{N}{M} \geq 2d(2MNr)^t$, which is equivalent to $N \geq (2^{1+t} M^{1+t} dr^t)^{\frac{1}{1-t}}$, then for each (a, θ, b) of interest, there is at most one $n \in \mathbb{Z}^2$ such that

$$|A_a^{-1} R_\theta^{-1} (a \cdot e_\theta - N \nabla(n^T F \phi(b)))| \leq d.$$

This implies that $\{Z_n\}$ are disjoint sets. Notice that $\hat{w}(x)$ decays when $|x| \geq d$. The above statement also indicates that there is at most one $n \in \Gamma_{a\theta}$ such that

$$f_n(b) \hat{w}(A_a^{-1} R_\theta^{-1} (a \cdot e_\theta - N |n^T F| \nabla \tilde{\phi}_n(b))) \neq 0.$$

Hence, if $(a, \theta, b) \in R_\epsilon$, there must be some n such that $\hat{S}(n) \neq 0$ and

$$(7) \quad W_f(a, \theta, b) = a^{-\frac{s+t}{2}} (f_n(b) \hat{w}(A_a^{-1} R_\theta^{-1} (a \cdot e_\theta - N |n^T F| \nabla \tilde{\phi}_n(b))) + \mathcal{O}(\epsilon)).$$

By the definition of Z_n , we see $(a, \theta, b) \in Z_n$. So, $R_\epsilon \subset \bigcup_{\hat{S}(n) \neq 0} Z_n$ and (1) is proved.

Now, we estimate $\nabla_b W_f(a, \theta, b)$. Suppose $(a, \theta, b) \in R_\epsilon \cap Z_n$. Similarly to the estimate of $W_f(a, \theta, b)$, by Lemma 2, there exists $N_2(M, s, t, d, \epsilon)$ such that if $N > N_2$ then

$$\begin{aligned} & \nabla_b W_f(a, \theta, b) \\ &= a^{-\frac{s+t}{2}} \left(2\pi i N \sum_{n \in \Gamma_{a\theta}} |n^T F| \nabla \tilde{\phi}_n(b) f_n(b) \hat{w}(A_a^{-1} R_\theta^{-1} (a \cdot e_\theta - N |n^T F| \nabla \tilde{\phi}_n(b))) + \mathcal{O}(\epsilon) \right) \\ &= a^{-\frac{s+t}{2}} (2\pi i N |n^T F| \nabla \tilde{\phi}_n(b) f_n(b) \hat{w}(A_a^{-1} R_\theta^{-1} (a \cdot e_\theta - N |n^T F| \nabla \tilde{\phi}_n(b))) + \mathcal{O}(\epsilon)) \end{aligned}$$

for the same n in (7).

Let $g = f_n(b) \hat{w}(A_a^{-1} R_\theta^{-1} (a \cdot e_\theta - N |n^T F| \nabla \tilde{\phi}_n(b)))$, then

$$v_f(a, \theta, b) = \frac{N |n^T F| \nabla \tilde{\phi}_n(b) g + \mathcal{O}(\epsilon)}{g + \mathcal{O}(\epsilon)}.$$

Since $|W_f(a, \theta, b)| \geq a^{-\frac{s+t}{2}} \sqrt{\epsilon}$ for $(a, \theta, b) \in R_\epsilon$, then $|g| \gtrsim \sqrt{\epsilon}$. So

$$\begin{aligned} \frac{|v_f(a, \theta, b) - N \nabla(n^T F \phi(b))|}{|N \nabla(n^T F \phi(b))|} &= \frac{|v_f(a, \theta, b) - N |n^T F| \nabla \tilde{\phi}_n(b)|}{|N |n^T F| \nabla \tilde{\phi}_n(b)|} \\ &\lesssim \left| \frac{\mathcal{O}(\epsilon)}{g + \mathcal{O}(\epsilon)} \right| \\ &\lesssim \sqrt{\epsilon}. \end{aligned}$$

The above estimate holds for $N > N_0 = \max\{N_1, N_2, (2^{1+t} M^{1+t} dr^t)^{\frac{1}{1-t}}\}$. The proof is complete. \square

Theorem 8 indicates that the underlying wave-like components $\hat{S}(n) \alpha(x) e^{2\pi i N n^T F \phi(x)}$ of the 2D general intrinsic mode type function $f(x) = \alpha(x) S(2\pi N F \phi(x))$ are well-separated, if they are within a scale $a \leq 2MNr$ and N is sufficiently large. By the definition of the synchrosqueezed energy distribution, $T_f(a, \theta, b)$ would concentrate around their local wave vectors $N \nabla(n^T F \phi(b))$. The energy around each local wave vectors reflects the energy of the corresponding wave-like component by the norm equivalence (6).

In the crystal image analysis, grains would have local defects, irregular boundaries and smooth trends caused by reflection etc. First, it is important to know where we can keep the local wave vector estimates accurate. Suppose a 2D general intrinsic mode type function $\hat{S}(n) \alpha(x) e^{2\pi i N n^T F \phi(x)}$ is defined in a domain Ω with a boundary $\partial\Omega$. The smallest scale used to estimate local wave vectors is of order $\frac{N}{M}$. Hence, the general wave packets used have supports of size at most $\frac{M^t}{dN^t}$ by $\frac{M^t}{dN^t}$. Let us denote a perfect interior of Ω as

$$\tilde{\Omega} = \left\{ x \in \Omega : |x - y| > \frac{M^t}{dN^t}, \forall y \in \partial\Omega \right\},$$

then the estimates of local wave vectors remain accurate in $\tilde{\Omega}$. As the numerical results in [9, 33, 35, 36] show, synchrosqueezed transforms can still approximately recover instantaneous or local properties near $\partial\Omega$.

The second concern is the influence of the smooth trends $c_k(x)$ in (2). By the method of stationary phase, the Fourier transform $\hat{c}_k(\xi)$ would decay quickly as $|\xi|$ increases. Hence, the influence of smooth trends is essentially negligible when the synchrosqueezed transforms are applied to estimate local wave vectors $Nn^T F V \phi(x)$ with a sufficiently large wave number.

3. CRYSTAL DEFECT ANALYSIS ALGORITHMS AND IMPLEMENTATIONS

This section introduces several algorithms based on the features of crystal images and 2D synchrosqueezed transforms for a fast analysis of local defects, crystal rotations and deformations. As discussed in the introduction, we will focus on the analysis of an image with only one type of crystals, i.e., suppose

$$\begin{aligned} f(x) &= \sum_{k=1}^M \chi_{\Omega_k}(x) (\alpha_k(x) S(2\pi N F \phi_k(x)) + c_k(x)) \\ &= \sum_{k=1}^M \chi_{\Omega_k}(x) \left(\sum_{n \in \mathbb{Z}^2} \hat{S}(n) \alpha_k(x) e^{2\pi i N n^T F \phi(x)} + c_k(x) \right). \end{aligned}$$

In the 2D space domain, there are five kinds of Bravais lattices, which are oblique, rectangular, centered rectangular (rhombic), hexagonal, and square [19] as shown in Figure 2. Accordingly, there are five kinds of 2D Fourier power spectra $|\hat{S}(n)|$. These spectra have a few dominant wave vectors in terms of energy, i.e., a few $|\hat{S}(n)|$ with large values. At each interior point of a grain, a sufficiently localized Fourier transform is able to recover an approximate distribution of the 2D Fourier power spectrum, based on which the corresponding reference configuration of this grain can be specified. Hence, for the simplicity of a presentation, we will restrict ourselves to the analysis of images of hexagonal crystals (e.g. Figure 3 (left)). A generalization of our algorithms to other kinds of simple crystal images is straightforward. In the case of a complex lattice, there might be numerous local wave vectors with relatively large energy. Feature extraction and dimension reduction techniques should be applied to provide a few crucial local wave vectors. This would be an interesting future work.

We will introduce two fast algorithms for crystal image analysis. Algorithm *A* provides estimates of grain boundaries and crystal rotations; while Algorithm *B* further identifies point defects, dislocations, and deformations. To make our presentation more transparent, the algorithms and implementations are introduced with toy examples. For Algorithm *A*, we will use the example in Figure 3 (left) which contains two undeformed grains with a straight grain boundary. While Figure 3 is a synthetic example, it illustrates nicely the key feature of atomic crystal images and the idea of local phase plane spectrum. In this example, the reciprocal lattice parameter $N = 120$ and the crystal rotations are given by 15 and 52.5 degrees on the left and right respectively. We introduce Algorithm *B* using strained examples of a small angle boundary (see Figure 6 (left)) and with some isolated dislocations (see Figure 6 (right)). These are examples from phase field crystal simulations [13].

3.1. Frequency band detection (bump detection).

Typically, each grain

$$\chi_{\Omega_k}(x) (\alpha_k(x) S(2\pi N F \phi_k(x)) + c_k(x))$$

in a polycrystalline crystal image can be identified as a 2D general intrinsic mode type function of type (M, N, F) with a small M near 1, unless the strain is too large. Hence, the 2D Fourier power spectrum of a multi-grain image would have several well-separated nonzero energy annuli centered at the origin due to

crystal rotations (see an example shown in Figure 3 (middle)). Suppose the radially average Fourier power spectrum is defined as

$$E(r) = \frac{1}{r} \int_0^{2\pi} |\hat{f}(r, \theta)| d\theta,$$

where $\hat{f}(r, \theta)$ is the Fourier transform in the radial coordinate: $\hat{f}(r, \theta) = \hat{f}(\xi)$ and $\xi = (r \cos(\theta), r \sin(\theta))^T \in \mathbb{R}^2$. Then $E(r)$ would have several well-separated energy bumps (see Figure 3 (right)) for the same reason.

As we can see in Figure 3 (middle), a hexagonal crystal image with a single grain

$$f(x) = \alpha(x)S(2\pi NF\phi(x)) + c(x)$$

has six dominant local wave vectors close to $v_j(\theta(x))$, $j = 0, 1, \dots, 5$, which are the vertices of a hexagon centered at the origin in the Fourier domain, i.e.,

$$v_j(\theta(x)) = \left(N \cos(\theta(x) + \frac{j\pi}{3}), N \sin(\theta(x) + \frac{j\pi}{3}) \right)^T, \quad j = 0, 1, \dots, 5,$$

for $\theta(x) \in [0, \frac{\pi}{3}]$. Suppose $S(2\pi NF(x))$ is a reference configuration, then the local rotation function with respect to each vertex $v_j(0)$ is

$$(8) \quad \beta(f)(x) \approx \arg(v_j(\theta(x))) - \arg(v_j(0)) = \theta(x).$$

Actually, $f(x)$ can approximately be considered as a rotated version of $\alpha S(2\pi NF(x+z)) + c$ by an angle $\theta(x) + \frac{k\pi}{3}$ for any $k \in \mathbb{Z}$ due to the crystal symmetry. The restriction $\theta(x) \in [0, \frac{\pi}{3}]$ guarantees a unique local rotation function $\beta(f)(x)$.

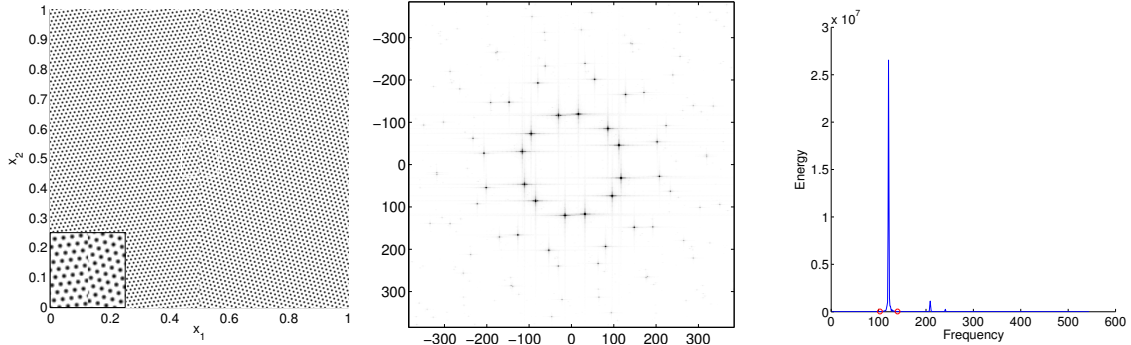


FIGURE 3. Left: An undeformed example of two hexagonal grains with a vertical line boundary. Middle: Its Fourier power spectrum. The number of dominant local wave vectors is 12 due to the superposition of spectrum of the two grains. Right: Its radially average Fourier power spectrum with the identified most dominant energy bump indicated by two red circles.

The discussion above shows that it is sufficient to compute the local rotation function using the dominant local wave vectors. To reduce the computational cost of 2D SST, the support of the most dominant energy bump in the radially average Fourier power spectrum should be identified (see Figure 3 (right)). Suppose the support (i.e. frequency band) is $[r_1, r_2]$. Then a band-limited fast 2D SST as introduced later is applied to estimate the local wave vectors with wave numbers in $[r_1, r_2]$.

In what follows, we would walk through the steps to determine the dominant frequency band $[r_1, r_2]$ with a time complexity $O(L^2 \log L)$ for an L by L image. For simplicity, we consider images that are periodic over

the unit square $[0, 1]^2$ in $2D$. If it is not the case, the images will be periodized by padding zeros around the image boundary. Let

$$X = \{(n_1/L, n_2/L) : 0 \leq n_1, n_2 < L, n_1, n_2 \in \mathbb{Z}\}$$

be the $L \times L$ spatial grid at which crystal image functions are sampled. The corresponding $L \times L$ Fourier grid is

$$\Xi = \{(\xi_1, \xi_2) : -L/2 \leq \xi_1, \xi_2 < L/2, \xi_1, \xi_2 \in \mathbb{Z}\}.$$

For a function $f(x) \in \ell^2(X)$, we apply the $2D$ FFT to obtain $\hat{f}(\xi) \in \ell^2(\Xi)$ first. Then the energy $|\hat{f}(\xi)|$ should be stacked up and averaged to obtain the radially average Fourier power spectrum $E(r)$. To realize this step, a grid of step size Δ is generated to discretize the domain $[0, \infty)$ in variable r as follows:

$$R = \{n\Delta : n \in \mathbb{N}\}.$$

At each $r = n\Delta \in R$, we associate a cell D_r started at r

$$D_r = [n\Delta, (n+1)\Delta).$$

Then $E(r)$ is estimated by

$$E(r) = \frac{1}{r} \sum_{\xi \in \Xi : |\xi| \in D_r} |\hat{f}(\xi)|.$$

The component task to identify the most dominant energy bump in $E(r)$ here belongs to a simple case of geometric object identification problems which have been extensively studied in [2, 15, 16, 37]. For a $1D$ discrete signal of length L , it has been proved that the optimal complexity to detect bumps in this signal is $O(L)$ in [2]. Since $E(r)$ has only a few well-separated and sharp energy bumps with relatively small noise, we would adopt the following straightforward but still effective algorithm with $O(L)$ complexity to detect the most dominant energy bump in $E(r)$.

Algorithm 9. Bump detection algorithm

- 1: *Input:* Vector $E = (E_i)$, $i = 0, \dots, L - 1$, parameters c_1 and c_2 .
- 2: *Output:* End points of the identified bump r_1 and r_2 .
- 3: **function** BumpDetection(E, c_1, c_2)
- 4: Find p_0 s.t. $E_{p_0} = \max_i E_i$ and set up a threshold $\delta = E_{p_0} c_1$.
- 5: Compute $\tilde{E}_i = \min(E_i, \delta)$ for $i = 1, \dots, L - 1$.
- 6: Find the largest $p_2 < p_0$ s.t. $\tilde{E}_{p_2} \geq \tilde{E}_{p_2+1}$. If p_2 does not exist, let $p_2 = 0$.
- 7: Find the largest $p_1 < p_0$ s.t. $\tilde{E}_{p_1} > \tilde{E}_{p_1+1}$. If p_1 exists, let $r_1 = (p_1 + p_2)/2$. Otherwise, let $r_1 = p_2$.
- 8: Find the smallest $p_1 > p_0$ s.t. $\tilde{E}_{p_1} \geq \tilde{E}_{p_1-1}$. If p_1 does not exist, let $p_1 = L - 1$.
- 9: Find the smallest $p_2 > p_0$ s.t. $\tilde{E}_{p_2} > \tilde{E}_{p_2-1}$. If p_2 exists, let $r_2 = (p_1 + p_2)/2$. Otherwise, let $r_2 = p_1$.
- 10: Let $r_1 = \max\{0, r_1(1 - c_2)\}$ and $r_2 = \min\{L - 1, r_2(1 + c_2)\}$.
- 11: **return** $[r_1, r_2]$
- 12: **end function**

When the dominant energy bump is located in the low frequency part, i.e. $r_1 = 0$, the energy comes from the smooth trend functions of the crystal image. Hence, it is reasonable to eliminate this bump from $E(r)$ and apply Algorithm 9 again to update new $[r_1, r_2]$, which is the frequency band of dominant local wave vectors. Since the complexity of each searching procedure is at most $O(L)$, the complexity of Algorithm 9 is $O(L)$. Because the time complexity of $2D$ FFT is $O(L^2 \log L)$, the total time complexity for frequency band detection is $O(L^2 \log L)$.

3.2. Band-limited 2D fast SST. The 2D synchrosqueezed transforms were originally proposed in [35, 36] for 2D mode decomposition problems. For an image of size L by L , the time complexity for these transforms is $O(L^{2+t-s} \log(N))$, where t and s are the geometric scaling parameters for the general wave packet transforms. To reduce the complexity, a band-limited 2D fast SST is introduced following a similar methodology to estimate local wave vectors with wave numbers in $[r_1, r_2]$ provided by the frequency band detection.

The band-limited 2D SST is based on a band-limited 2D general wave packet transform. The key idea is to restrict the class of general wave packets

$$\{w_{a\theta b}(x), a \in [1, \infty), \theta \in [0, 2\pi), b \in \mathbb{R}^2\}$$

to a band-limited class

$$\{w_{a\theta b}(x), a \in [r_1, r_2], \theta \in [0, 2\pi), b \in \mathbb{R}^2\}.$$

Meanwhile, a discrete analog of the band-limited class of general wave packets is constructed by specifying a set of tilings covering the annulus $\{\xi \in \mathbb{R}^2 : r_1 \leq |\xi| \leq r_2\}$. To be more specific, we need to specify how to decimate the Fourier domain (a, θ) and the position space b as follows.

In the Fourier domain, the decimation follows two steps. First, we follow the discretization and construction of the discrete general curvelet transform in [36] to construct the discrete general wave packets here. Notice that the support parameter d in [36] is 1. The sizes of tilings in this paper should be multiplied by d . Second, we keep those discrete general wave packets with supports overlapping the annulus $\{\xi \in \mathbb{R}^2 : r_1 \leq |\xi| \leq r_2\}$ to obtain the band-limited class of discrete general wave packets.

To decimate the position space b , we discretize it with an $L_B \times L_B$ uniform grid:

$$B = \{(n_1/L_B, n_2/L_B) : 0 \leq n_1, n_2 < L_B, n_1, n_2 \in \mathbb{Z}\}.$$

It is required that L_B is large enough so that a sampling grid of size $L_B \times L_B$ can cover the supports of general wave packets of interest in the Fourier domain. For a crystal image

$$f(x) = \sum_k \chi_{\Omega_k}(x) (\alpha_k(x) S(2\pi N F \phi_k(x)) + c_k(x))$$

defined in $[0, 1]^2$, its fundamental wave number is $O(N)$, i.e., $r_1 = O(N)$ and $r_2 = O(N)$. Hence, the largest support of general wave packets in the Fourier domain is of size $O(N^t)$, implying that L_B is at least $O(N^t)$.

With the band-limited class of general wave packets ready, we follow the fast algorithms in [36] to compute the forward general wave packet transform $W_f(a, \theta, b)$, the local wave vector estimate $v_f(a, \theta, b)$ and the synchrosqueezed energy distribution $T_f(a, \theta, b)$. Notice that the width of the frequency band $r_2 - r_1 = O(1)$ compared to the fundamental wave number, which implies that the cardinality of the band-limited class is $O(N^{1-s})$. A straightforward calculation shows that the time complexity of the band-limited general wave packet transform is $O(L^2 \log L + N^{1-s} L_B^2 \log L_B)$. Because the synchrosqueezing procedure takes a complexity of $O(N^{1-s} L_B^2)$, the total time complexity for the band-limited 2D fast SST is $O(L^2 \log L + N^{1-s} L_B^2 \log L_B)$.

As an example, Figure 4 shows the synchrosqueezed energy distribution $T_f(a, \theta, b)$ in a polar coordinate at three different positions. Because the crystal image is real, it is enough to compute the synchrosqueezed energy distribution for $\theta \in [0, \pi]$. The results show that the essential support of $T_f(a, \theta, b)$ can accurately estimate local wave vectors when location b is not at the boundary. When b is at the boundary, the essential support of $T_f(a, \theta, b)$ can still provide some information, e.g. crystal rotations.

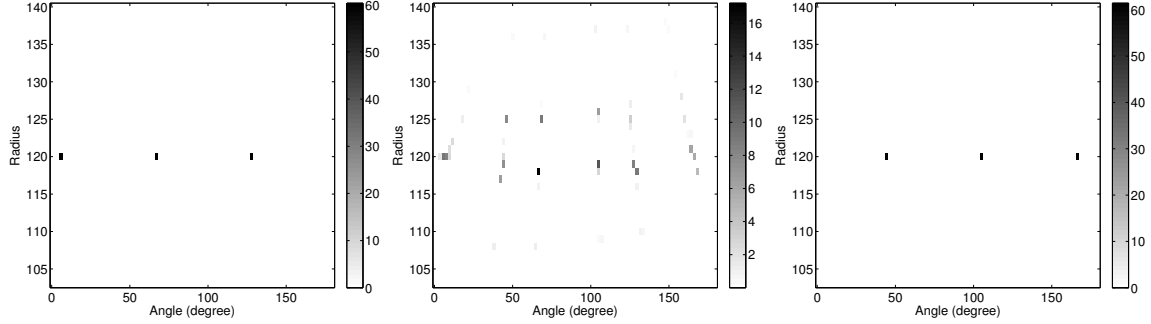


FIGURE 4. The synchrosqueezed energy distribution $T_f(a, \theta, b)$ of Figure 3 (left) at three different points b_i , $i = 1, 2, 3$. Left: $b_1 = (0.25, 0.5)$ is in the middle of the left grain. Middle: $b_2 = (0.5, 0.5)$ is at the boundary. Right: $b_3 = (0.75, 0.5)$ is in the middle of the right grain. Note that the scale of colorbar is different in the middle panel.

3.3. Defect detection algorithms. As we can see in Figure 4, the synchrosqueezed energy around each local wave vector $\nabla(Nn^T F\phi(x))$ is stable and of order $|\widehat{S}(n)|\alpha_k(x)$ when x is in the perfect interior $\widetilde{\Omega}_k$. Moreover, the energy would decrease fast near the boundary $\partial\Omega_k$ and becomes zero soon outside Ω_k . This motivates the application of synchrosqueezed energy distribution to identify grain boundaries by detecting the irregularity of energy distribution as follows.

Algorithm A (Fast defect detection algorithm based on stacked synchrosqueezed energy).

Step 1: Stack the synchrosqueezed energy distribution and define a stacked synchrosqueezed energy distribution as

$$\tilde{T}_f(a, \theta, b) = T_f(a, \theta, b) + T_f(a, \theta + \frac{\pi}{3}, b) + T_f(a, \theta + \frac{2\pi}{3}, b)$$

for $\theta \in [0, \frac{\pi}{3}]$.

Step 2: Compute an angular total energy distribution

$$E_a(\theta, b) = \int_{r_1}^{r_2} \tilde{T}_f(a, \theta, b) da.$$

Step 3: For each b , apply Algorithm 9 to identify the most dominant energy bump in $E_a(\theta, b)$. Denote the range of this bump as $[\theta_{11}(b), \theta_{12}(b)]$.

Step 4: Compute the total energy of the first identified bump as

$$TE_1(b) = \int_{\theta_{11}(b)}^{\theta_{12}(b)} E_a(\theta, b) d\theta.$$

Step 5: Compute a weighted average angle of the first bump as

$$\text{Angle}(b) = \frac{1}{TE_1(b)} \int_{\theta_{11}(b)}^{\theta_{12}(b)} E_a(\theta, b) \theta d\theta.$$

Step 6: For each b , update E_a such that $E_a(\theta, b) = 0$, if $\theta \in [\theta_{11}(b), \theta_{12}(b)]$. Apply Algorithm 9 again to update the most dominant energy bump in E_a . Denote the range of this bump as $[\theta_{21}(b), \theta_{22}(b)]$.

Step 7: Compute the total energy of the second identified bump by

$$TE_2(b) = \int_{\theta_{21}(b)}^{\theta_{22}(b)} E_a(\theta, b) d\theta.$$

Step 8: Compute the boundary indicator function

$$BD(b) = \frac{1}{\sqrt{TE_1(b) - TE_2(b) + 1}}.$$

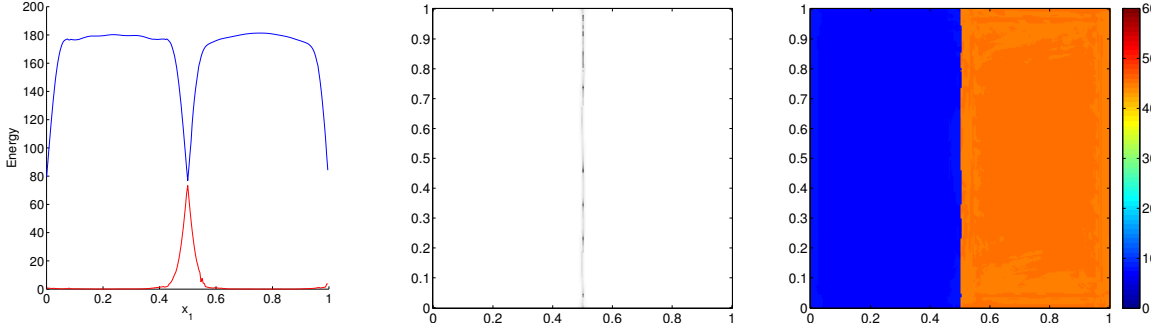


FIGURE 5. Left: The total energy function $TE_1(b)$ in blue and $TE_2(b)$ in red for fixed $b_2 = 0.5$. Middle: The boundary indicator function $BD(b)$. Right: The weighted average angle $\text{Angle}(b)$ as an approximation of crystal rotations. The real crystal rotations are 15 degrees on the left and 57.5 degrees on the right.

The synchrosqueezed energy distribution of each grain behaves like an energy bump essentially supported in Ω_k and quickly decays outside Ω_k . Hence, two energy bumps have close energy in the transition area containing the grain boundary. Since $TE_1(b)$ acts as the maximum of two energy distributions and $TE_2(b)$ acts as the minimum (see Figure 5 (left)), $TE_1(b) - TE_2(b)$ decays near the grain boundary and the boundary indicator function $BD(b)$ is relatively large at the grain boundary. As Figure 5 (middle) shows, the grain boundary can be identified from a grayscale image of $BD(b)$.

By the discussion in Section 3.1, the local rotation function with respect to each local wave vector of the reference hexagonal configuration are approximately the same. Since, the synchrosqueezed energy distribution $T_f(a, \theta, b)$ is stacked together per $\frac{\pi}{3}$ in θ , the weighted average $\text{Angle}(b)$ approximates the local rotation functions in a weighted average sense. As shown in Figure 5 (right), $\text{Angle}(b)$ accurately reflects the crystal rotations in this example.

As discussed in Section 3.1 and 3.2, before Algorithm *A*, it takes $O(L^2 \log L + N^{1-s} L_B^2 \log L_B)$ time complexity to estimate the frequency band $[r_1, r_2]$ and to compute $T_f(a, \theta, b)$. Suppose that the discrete grid of $T_f(a, \theta, b)$ at each b is of size $L_R \times L_A$, then the time complexity of Algorithm *A* is $O(L_A L_R L_B^2)$. Hence, the total complexity for the crystal analysis is $O(L^2 \log L + N^{1-s} L_B^2 \log L_B + L_A L_R L_B^2)$.

The stacking step in Algorithm *A* is averaging the influence of each local wave vector. This gives a stable result of grain boundary and crystal rotation estimates even with severe noise as will be illustrated in Section 4. However, Algorithm *A* might miss some local defects that would not influence all local wave vectors simultaneously. For example, in Figure 6 (left), two of the underlying wave-like components have smoothly changing directions, while the third one changes its direction suddenly at a line segment, resulting in a small angle boundary. At some local dislocations, as Figure 6 (right) shows, the dislocation might not cause irregularity to all wave-like components. Hence, to be more sensitive to local irregularity, it is reasonable to remove the stacking step in Algorithm *A*, if noise is relatively small. This motivates the following algorithm.

Algorithm B (Fast defect detection algorithm with enhanced sensitivity).

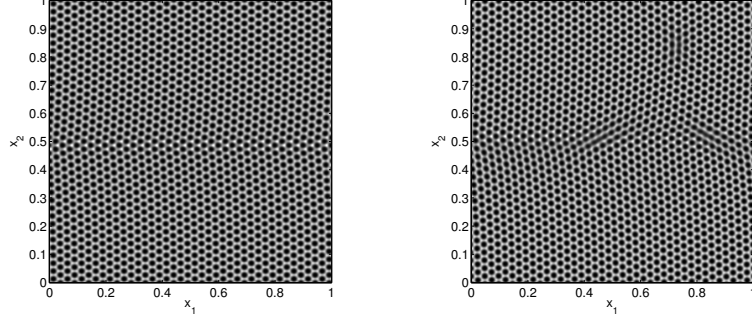


FIGURE 6. Left: An example of a small angle boundary. Right: An example of some isolated dislocations. Courtesy of Benedikt Wirth. The sizes of these images are 512×512 pixels.

Step 1: Define $\tilde{T}_j(a, \theta, b) = T_f(a, \theta + j\pi/3, b)$ for $\theta \in [0, \frac{\pi}{3})$ and $j = 0, 1, 2$. Apply Steps 2 – 8 in Algorithm A to $\tilde{T}_j(a, \theta, b)$ to compute $TE_{1j}(b)$, $TE_{2j}(b)$, $Angle_j(b)$ and $BD_j(b)$ for each j .

Step 2: For each $j = 0, 1, 2$, compute the weight function

$$W_j(b) = \frac{TE_{1j}(b) + TE_{2j}(b)}{\sum_j (TE_{1j}(b) + TE_{2j}(b))}.$$

Step 3: Compute the weighted average angle

$$Angle(b) = \sum_j W_j(b) Angle_j(b).$$

Step 4: Compute the weighted boundary indicator function

$$BD(b) = \sum_j W_j(b) BD_j(b).$$

In the example in Figure 6 (left), only the second local wave vector exhibits irregularity at the small angle boundary, resulting in a sharp decrease of $TE_{11}(b)$ and a sharp increase of $TE_{21}(b)$ at the boundary. Hence, as shown in Figure 7, the weighted boundary indicator function $BD(b)$ with $BD_1(b)$ as a key integrand can clearly indicate the small angle boundary. As Figure 8 shows, the top point dislocation in the example in Figure 6 (right) interrupts the first and third underlying wave-like component, resulting in a sharp decrease in $TE_{10}(b)$ and $TE_{12}(b)$ and a sharp increase in $TE_{20}(b)$ and $TE_{22}(b)$. Therefore, the weighted boundary indicator function can reveal this point dislocation. The results in Figure 7 and 8 indicates that the information of some local defects is hidden behind some particular local wave vectors. By using the synchrosqueezed energy distribution of each local wave vector individually, more information of local defects can be discovered.

3.4. Recovery of local deformation gradient. In addition to grain boundaries and crystal rotations, a reliable extraction of the elastic deformation of a crystal image is also essential for an efficient material characterization. Instead of estimating the elastic deformation $\phi(x)$ directly, we would emphasize how to recover the local deformation gradient

$$\nabla\phi(x) = \begin{pmatrix} \partial_{x_1}\phi_1(x) & \partial_{x_2}\phi_1(x) \\ \partial_{x_1}\phi_2(x) & \partial_{x_2}\phi_2(x) \end{pmatrix},$$

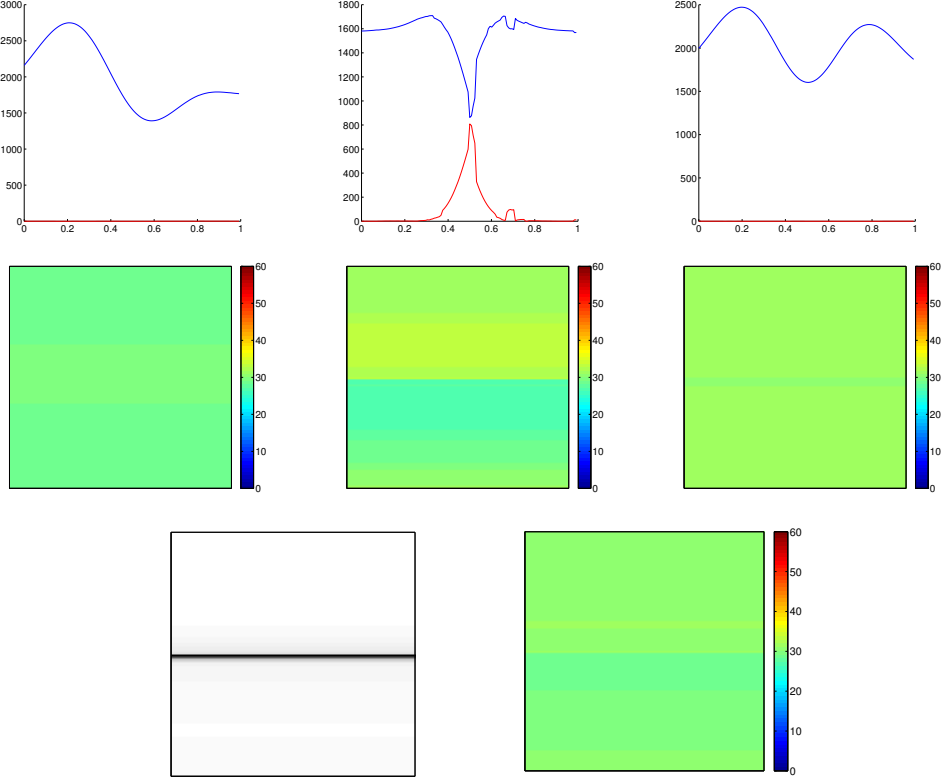


FIGURE 7. Top: $\text{TE}_{1j}(b)$ (in blue) and $\text{TE}_{2j}(b)$ (in red) of Figure 6 (left) for fixed $b_1 = 0.5$ and $j = 0, 1, 2$ from left to right, respectively. Center: The weighted average angle functions $\text{Angle}_j(b)$ provided by each local wave vector for $j = 0, 1, 2$, respectively. Bottom left: the weighted boundary indicator function $\text{BD}(b)$. Bottom right: the weighted average angle function $\text{Angle}(b)$.

and how to read more information from $\nabla\phi(x)$, e.g., directions of Burgers vectors.

The estimation of the local deformation gradient $\nabla\phi(x)$ relies on the complete estimate of at least two local wave vectors $\nabla(Nn^T F\phi(x))$. Let us continue with hexagonal crystal images as an example. In this case, there are six local wave vectors of interest as discussed in Section 3.1. By symmetry, it is enough to consider those in the upper half plane of the Fourier domain. They are

$$\nu_j(x) = (\nabla\phi(x))^T \left(N \cos\left(\frac{j\pi}{3}\right), N \sin\left(\frac{j\pi}{3}\right) \right)^T, \quad j = 0, 1, 2.$$

In Algorithm *B*, the argument of each $\nu_j(x)$ has been estimated by the weighted average angle $\text{Angle}_j(b)$. Similarly, one more step for applying the bump detection algorithm radially can provide a fast estimate of the length of $\nu_j(x)$. Suppose $\tilde{\nu}_j(x)$ is an estimate of $\nu_j(x)$ obtained by the fast algorithms above, then we have an over-determined linear system at each x

$$\tilde{\nu}_j(x) \approx (\nabla\phi(x))^T \left(N \cos\left(\frac{j\pi}{3}\right), N \sin\left(\frac{j\pi}{3}\right) \right)^T, \quad j = 0, 1, 2.$$

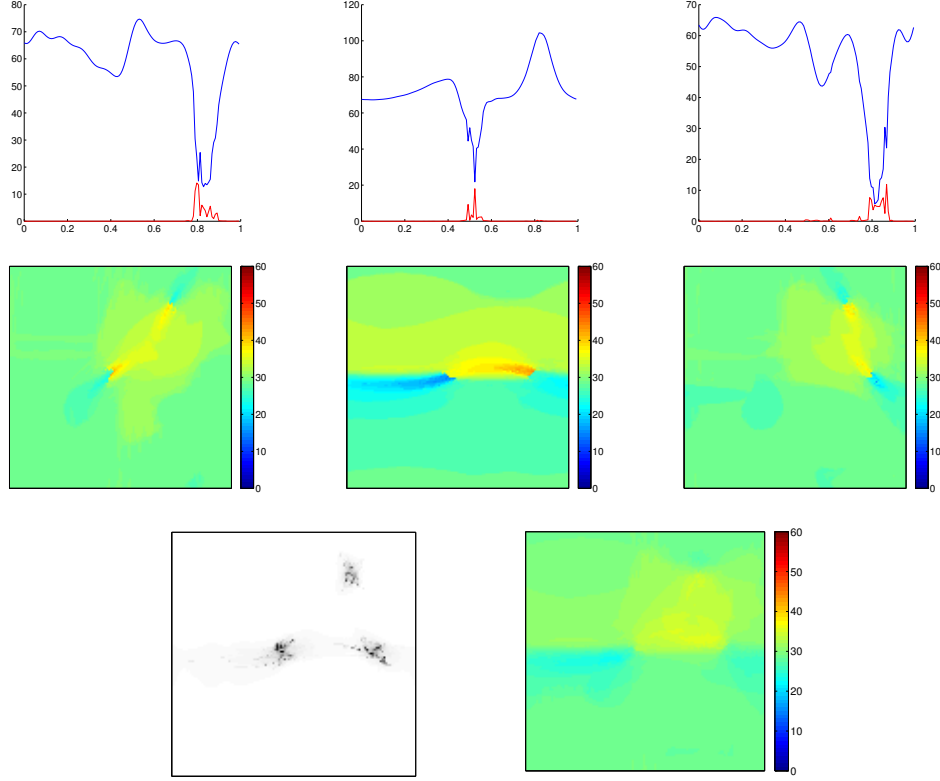


FIGURE 8. Top: $\text{TE}_{1j}(b)$ (in blue) and $\text{TE}_{2j}(b)$ (in red) of Figure 6 (right) for fixed $b_1 = 0.8$ and $j = 0, 1, 2$, respectively. Center: The weighted average angle functions $\text{Angle}_j(b)$ provided by each local wave vector for $j = 0, 1, 2$, respectively. Bottom left: the weighted boundary indicator function $\text{BD}(b)$. Bottom right: the weighted average angle function $\text{Angle}(b)$.

Notice that the reciprocal number N can be estimated by $\arg \max E(r)$, where $E(r)$ is the radially average Fourier power spectrum of the given crystal image. Hence, a least square method is sufficient to provide a good estimate $\nabla \tilde{\phi}(x)$ of the local deformation gradient $\nabla \phi(x)$.

As an example of reading information from the local deformation gradient $\nabla \phi(x)$, a local volume distortion estimate of $\det(\nabla \phi(x)) - 1$ is computed by

$$\text{Vol}(x) = \det \left(\frac{\nabla \tilde{\phi}(x)}{\int_{\Omega} \det(\nabla \tilde{\phi}(x)) dx / |\Omega|} \right) - 1,$$

where Ω is the domain of the crystal image and $|\Omega|$ denotes its area. The normalization reduces the influence of the estimate error of N . In the presence of a lattice distortion of a dislocation, a Burgers vector is introduced to represent this distortion. On one side of a Burgers vector, the space between atoms is slightly compressed, while the space on the other side is expanded. Hence, the local volume distortion would be positive on one side of the Burgers vector and negative on the other side. Suppose $\text{Vol}(x_1)$ and $\text{Vol}(x_2)$ are the maximum and the minimum of $\text{Vol}(x)$ in a local region near the dislocation. Then $\text{Vol}(x_1) - \text{Vol}(x_2)$ reflects the length of the Burgers vector and the vector $x_1 - x_2$ is orthogonal to the Burgers vector.

Figure 9 shows the local distortion volume estimate $\text{Vol}(x)$ of the example in Figure 6 (right). $\text{Vol}(x)$ reaches its local maximum and local minimum near each point dislocation and the direction of the corresponding Burgers vector can be directly read off from the color coding of $\text{Vol}(x)$. As a remark, $\text{Vol}(x)$ is not tightly supported around local dislocations in this example. This is because the synchrosqueezed transforms cannot be too localized in space and the estimate of $\nabla\phi(x)$ is polluted by the information at the other points nearby. We leave further regularization of these estimates to future works.

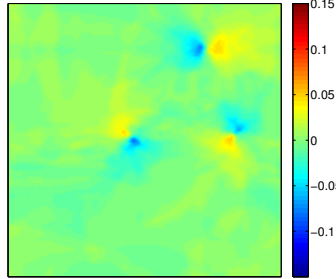


FIGURE 9. The local distortion volume $\text{Vol}(x)$ of the example in Figure 6 (right). To make the image more readable, the color limits of these two images are set to be 0.15 and -0.15 as the maximum and the minimum, respectively.

4. EXAMPLES AND DISCUSSIONS

This section contains a series of experiments of synthetic and real images to illustrate the performance of Algorithm *A* and *B*. In the first part of this section, we focus on the application of Algorithm *A* to detect grain boundaries and to estimate crystal rotations. The robustness of this method will be emphasized and supported by some noisy examples and examples with blurry grain boundaries. In the second part, Algorithm *B* is applied to two more examples with different types of point dislocations. Algorithm *B* is more sensitive to local defects and is able to discover Burgers vectors of these dislocations by estimating the local volume distortion $\text{Vol}(b)$. Throughout all examples, the threshold value ϵ for the synchrosqueezed transforms is 10^{-4} and other primary parameters such as s , t and d are application dependent. Generally speaking, large parameters s , t and d result in more sensitive synchrosqueezed transforms to local defects, while smaller parameters provide more stable analysis results.

Recall that both Algorithm *A* and *B* have a time complexity $O(L^2 \log L + N^{1-s} L_B^2 \log L_B + L_A L_R L_B^2)$. Since the time complexity depends on the reciprocal number N of a given crystal image and N is not known a priori, we would not emphasize the runtime taken to analyze images of different sizes. All the numerical results except for the one in Figure 15 and 16 take within 10 seconds using a Matlab code in a MacBook Pro with a 2.7GHz quad-core Intel Core i7 CPU. The result in Figure 15 and 16 takes about 50 seconds and the most expensive part is for the bump detection. The time expense will be reduced significantly by straightforward parallelization, though this is not our focus in this paper. The codes of these algorithms together with some numerical examples are open source and available as SynLab at <https://github.com/HaizhaoYang/SynLab>.

4.1. Examples for Algorithm A. Our first example is a phase field crystal (PFC) image in Figure 10 (left). It contains several grains with low and high angle grain boundaries and some point dislocations. As shown in Figure 10 (middle), the weighted average angle $\text{Angle}(b)$ is changing gradually in the interior of a grain and jumps at a large angle boundary. Figure 10 (right) shows the boundary indicator function $\text{BD}(b)$. Large angle grain boundaries appear in a form of line segments. Adjacent point dislocations are connected and identified as grain boundaries, while well-separated point dislocations are identified by light grey regions. As pointed out in Section 3, some isolated point dislocations may be missed due to the stacking step, while Algorithm B is better suited for detecting local defects, as will be shown in Figure 15 and Figure 18.

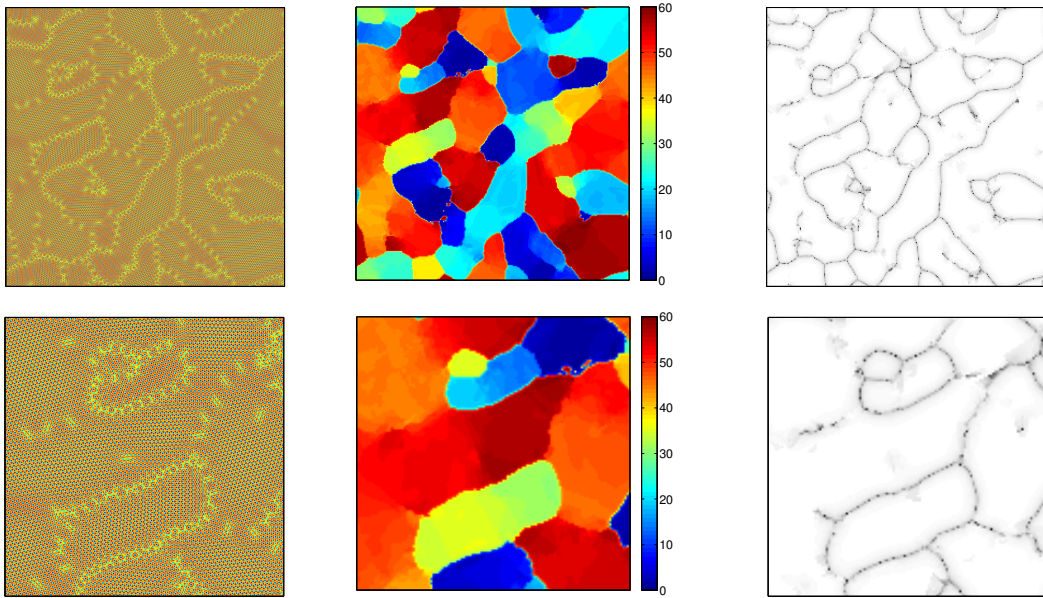


FIGURE 10. Analysis results of a large phase field crystal image (of size 1024×1024 pixels) provided by Algorithm A . The top row is the original image and the bottom row gives the zoomed-in view. Left: A phase field crystal (PFC) image and its zoomed-in image. Courtesy of Benedikt Wirth [14]. Middle: The weighted average angle $\text{Angle}(b)$ and its zoomed-in result. Right: The boundary indicator function $\text{BD}(b)$ and its zoomed-in result. Primary implementation parameters: $s = t = 0.5$, $d = 1$.

We next consider a real data example of a twin boundary in a TEM-image in GaN (see Figure 11 (left)). Algorithm A identifies two grains as shown in Figure 11 (middle) and estimates their rotation angles. The grain boundary is approximated by a smooth curve in the image of the boundary indicator function $\text{BD}(b)$ in Figure 11 (right).

Figure 12 shows an example of blurry boundaries in a photograph of a bubble raft. In this case, the transition between two grains is not sharp due to large distortion, in particular the local crystal structure is heavily disturbed near the boundary. Nevertheless, Algorithm A is capable of identifying three grains with sharp grain boundaries matching the distortion area as shown in Figure 12 (middle) and 12 (right).

To show the ability of our algorithm to analyze crystal images with strong illumination artifacts in the imaging like reflections and shadows, we analyze the example shown in Figure 13 (left), where the reflections and shadows exhibit strong spatial variations. Algorithm A identifies two grains as shown in Figure

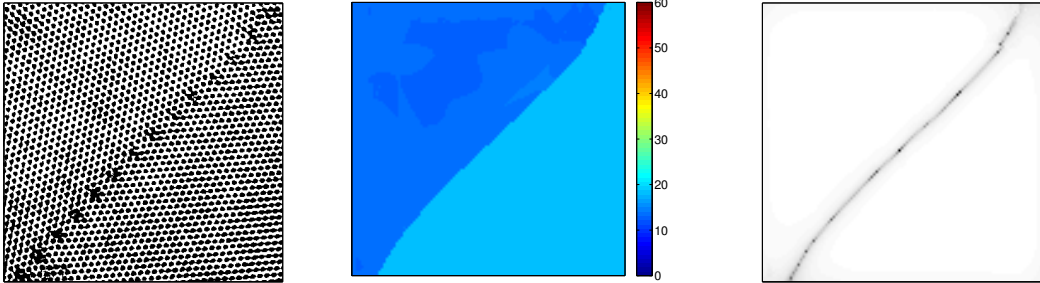


FIGURE 11. Left: A TEM-image of size 420×444 pixels in GaN. Courtesy of David M. Tricker (Department of Material Science and Metallurgy, University of Cambridge). Middle: The weighted average angle $\text{Angle}(b)$ provided by Algorithm A. Right: The boundary indicator function $\text{BD}(b)$ provided by Algorithm A. Primary implementation parameters: $s = t = 0.5$, $d = 0.5$.

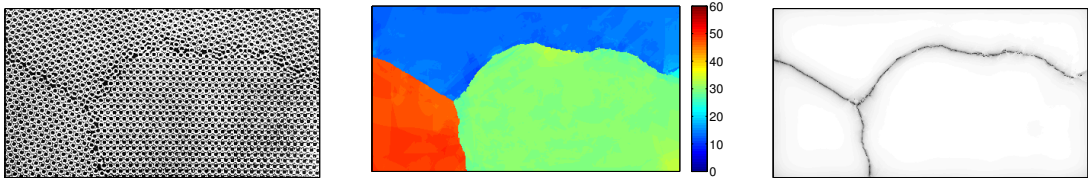


FIGURE 12. Left: A photograph of a bubble raft with large disorders and blurry boundaries. Courtesy to Barrie S. H. Royce in Princeton University. The image size is 223×415 . Middle and right: The weighted average angle $\text{Angle}(b)$ and the boundary indicator function provided by Algorithm A. Primary implementation parameters: $s = t = 0.5$, $d = 1$.

13 (middle). The weighted average angle $\text{Angle}(b)$ is slowly varying, indicating a smooth deformation over the domain. A large angle grain boundary consisting of an array of close point dislocations is identified by $\text{BD}(b)$ in Figure 13 (right). This example also shows that Algorithm A may miss isolated defects, which motivates the design of Algorithm B. We will revisit this example later with Algorithm B which will discover all the missing point defects.

Algorithm A also works robustly in noisy examples. A noisy example of a real atomic resolution image of a Sigma 99 tilt grain boundary in aluminum is shown in Figure 14 (a). The domain consists of three grains with fuzzy transition regions. This is a rather challenging example, as individual atoms are hardly identifiable in the middle-left part of the image. Grain boundaries by manual inspection are indicated in red in Figure 14 (g). The small region indicated by blue color contains a grain boundary that is hardly seen. The weighted average angle $\text{Angle}(b)$ provided by Algorithm A reveals three grains with slight deformation of lattices in Figure 14 (b). Grain boundaries can be also clearly seen from the boundary indicator function $\text{BD}(b)$ as shown in Figure 14 (c). They can be identified by a simple thresholding using $\text{BD}(b)$. Figure 14 (h) embeds the identified boundaries into the original crystal image. The result by manual inspection in Figure 14 (g) agrees with the one in Figure 14 (h).

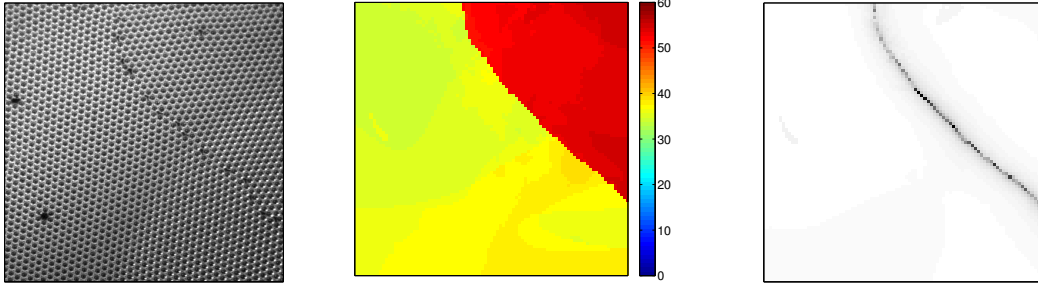


FIGURE 13. Left: A photograph of a bubble raft with strong reflections and point dislocations (courtesy to Don Stone, copyright 2009 Board of Regents of the University of Wisconsin System). Its size is 476×476 pixels. Middle and right: The weighted average angle $\text{Angle}(b)$ and the boundary indicator function provided by Algorithm *A*. Primary implementation parameters: $s = t = 0.5$, $d = 0.5$.

To demonstrate the robustness of our method, we normalize the image in Figure 14 (a) such that the maximum intensity is 1 and add Gaussian white noise with a standard deviation equal to 1. The polluted example is shown in Figure 14 (d). The atom structure is barely seen even away from the grain boundaries. The weighted average angle $\text{Angle}(b)$, the boundary indicator function $\text{BD}(b)$, and the estimated grain boundaries are shown in Figure 14 (e), (f), and (i). As shown by these results, Algorithm *A* is able to give similar results matching with the one by manual inspection even if noise is heavy.

4.2. Examples for Algorithm *B*. As pointed out previously, Algorithm *B* is more sensitive to local defects than Algorithm *A*. Therefore, it can better discover local defects hidden in the underlying wave-like components of crystal images. To validate this, let us revisit the phase field crystal image example shown in Figure 10. The analysis results are presented in Figure 15 and 16. First, as shown in Figure 15 (middle), the weighted average angle $\text{Angle}(b)$ provided by Algorithm *B* is consistent with the one by Algorithm *A*. Second, the boundary indicator function $\text{BD}(x)$ by Algorithm *B* reveals all local defects including grain boundaries and isolated dislocations clearly. As a trade off, Algorithm *B* visualizes grain boundaries as narrow fuzzy bands instead of sharp curves. Finally, as shown in Figure 16, isolated point dislocations appear as dipoles in the visualization of the local volume distortion $\text{Vol}(b)$. As a consequence, the Burgers vectors of corresponding isolated point dislocations can be inferred by the directions of these dipoles.

To demonstrate the robustness of Algorithm *B*, we normalize the intensity of the crystal image in Figure 15 and add Gaussian white noise with distributions $0.5\mathcal{N}(0, 1)$ and $1.4\mathcal{N}(0, 1)$. These noisy examples are shown in Figure 17 (a) and (d), respectively. In these heavily polluted cases, even when no crystal structure is clearly visible by human eyes, Algorithm *B* is still able to reveal grain boundaries and isolated defects with a reasonable accuracy (see Figure 17 (b) and (e)). The distortion volume in Figure 17 (c) and (f) still roughly reflects the strain stress encoded by color.

We also revisit the example shown in Figure 13 and apply Algorithm *B* to identify point defects. Different to the point dislocations in the previous phase field crystal example, some point defects here do not destroy the crystal lattice nearby. For example, the point defect in the bottom-left part of the bubble raft image looks like a missing bubble and it does not influence the positions of neighbor bubbles. Therefore, methods depending on identifying neighbor bubbles might fail to detect such a kind of local defects. Since missing

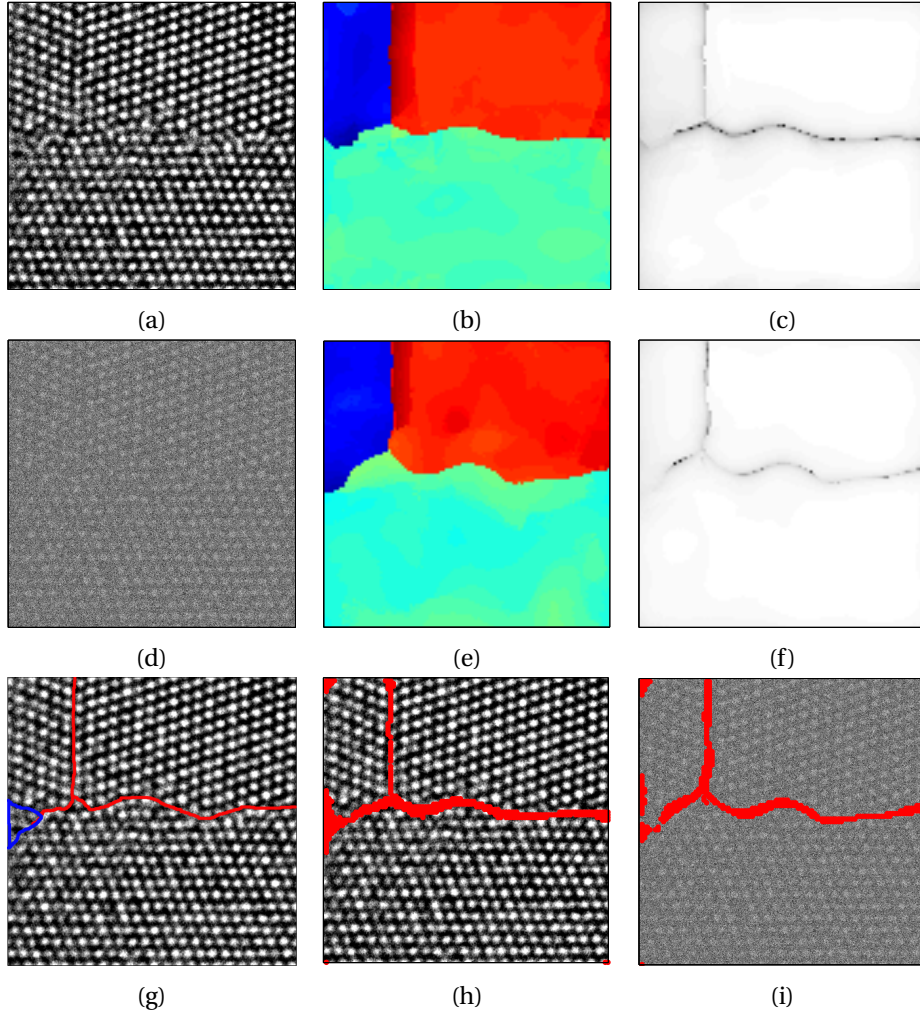


FIGURE 14. (a) and (d): An atomic resolution image of 424×424 pixels of Sigma 99 tilt grain boundary in Al and its noisy version. Courtesy of National Center for Electron Microscopy in Lawrence Berkeley National Laboratory. (b) and (e): The weighted average angle $\text{Angle}(b)$ of the images in (a) and (d), respectively. (c) and (f): The boundary indicator functions provided by Algorithm A for the images in (a) and (d), respectively. (g): The original crystal image associated with identified defect regions (in red) by manual inspection. The region indicated in blue contains a grain boundary that is hardly seen. (h) and (i): Identified defect regions (in red) by thresholding the boundary indicator function of (a) and (d), respectively. Primary implementation parameters: $t = 0.75$, $s = 0.65$, $d = 1$.

bubbles would reduce the synchrosqueezed energy at their places, Algorithm B is still able to detect them. As an illustration, Figure 18 shows the results provided by Algorithm B and the positions of those local defects in the left figure are accurately depicted in the right figure.

4.3. Quantitative analysis for statistical stability. We quantitatively analyze the performance of our algorithms in this subsection in terms of statistical stability using the example in Figure 15. Suppose $g = f + e$ is

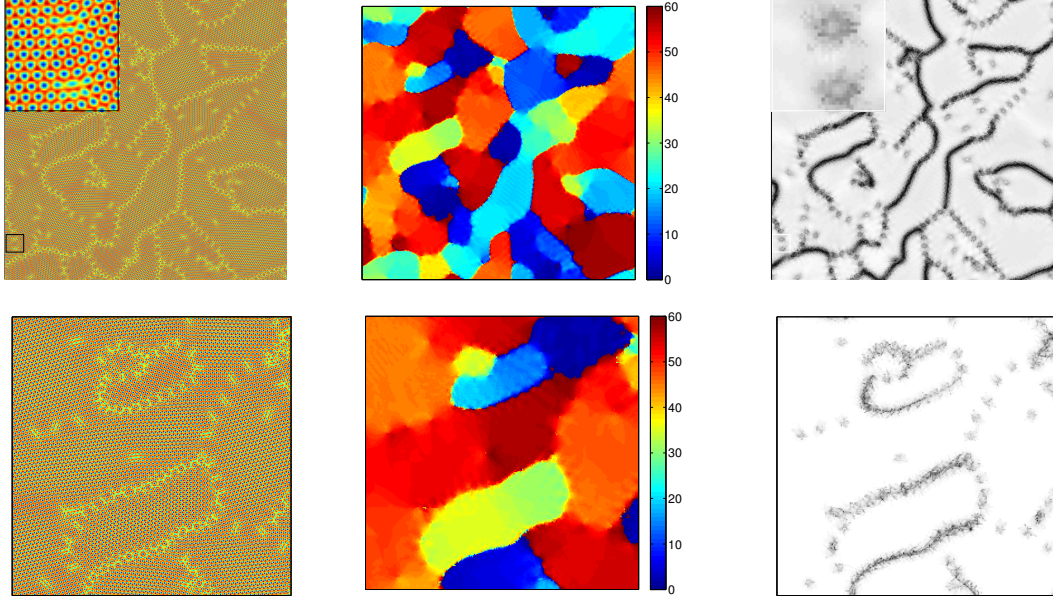


FIGURE 15. Analysis results of a phase field crystal image provided by Algorithm *B*. Compare with Figure 10. Left: A phase field crystal (PFC) image and its zoomed-in images. Middle: The weighted average angle $\text{Angle}(b)$ and its zoomed-in results. Right: The weighted boundary indicator function $\text{BD}(b)$ and its zoomed-in results. The small rectangles in the bottom-left corner of these images indicate the zoomed-in images in top-left corner. Primary implementation parameters: $s = t = 0.8$, $d = 1$.

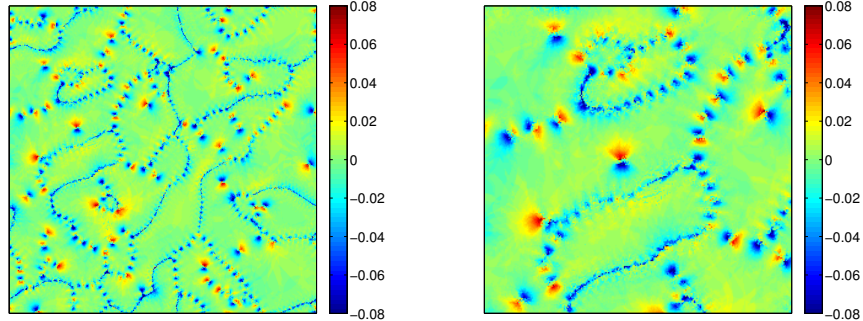


FIGURE 16. Left: The local volume distortion estimate $\text{Vol}(b)$ of the phase field crystal image example in Figure 15 and its zoomed-in result. The color limits of these two images are set to be 0.08 and -0.08 .

the noisy crystal image, where e is white Gaussian noise with a distribution $\sigma^2 \mathcal{N}(0, 1)$ and f is the noiseless crystal image. We introduce the signal-to-noise ratio (SNR) of the input data $g = f + e$ as follows:

$$\text{SNR}[dB](g) = 10 \log_{10} \left(\frac{\text{Var}(f)}{\text{Var}(e)} \right).$$

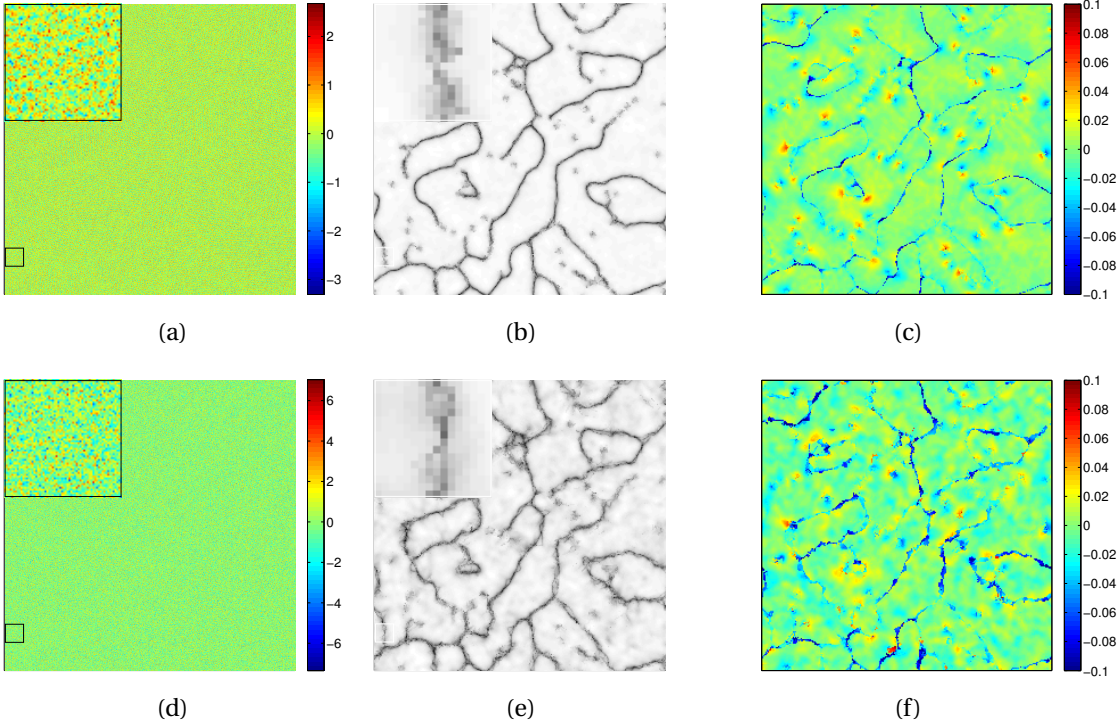


FIGURE 17. Analysis results of noisy phase field crystal images provided by Algorithm *B*. First row: Results of noisy data with Gaussian white noise $0.5\mathcal{N}(0,1)$. Second row: Results of noisy data with Gaussian white noise $1.4\mathcal{N}(0,1)$. First column: input images. Second column: detected grain boundaries and isolated defects. Third column: distortion volume. Zoomed-in images show that our method can still identify isolated defects even if noise is heavy.

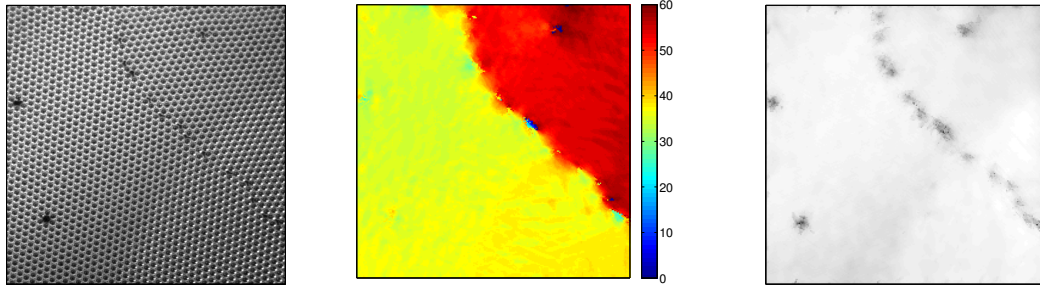


FIGURE 18. Revisit the example in Figure 13. Left: A photograph of a bubble raft with strong reflections and point dislocations. Middle and right: The weighted average angle $\text{Angle}(b)$ and the weighted boundary indicator function provided by Algorithm *B*. Primary implementation parameters: $s = t = 1$, $d = 1$.

We test Algorithm *A* and Algorithm *B* on these noisy examples with SNR's ranging from 35 to -10 . All results are summarized in Figure 19.

Since the ground truth for grain boundaries and the crystal rotations is not available, we compare the results of noisy examples with those in the noiseless case. To quantify the statistical stability of the grain boundary estimation, we apply the earth mover's distance (EMD) [22] to measure the distance between a boundary indicator function of a noisy example and the one of the noiseless example. The boundary indicator functions are converted to grayscale images. They can be considered as two-dimensional histograms describing the distribution of defects. At each pixel, the image intensity is from 0 to 255. One unit in the grayscale image is one unit of the mass of the distribution. The EMD in this paper is the total mass per pixel that we need to move from one distribution to match the other one. A smaller EMD indicates better statistical stability. Figure 19 (left) plots the EMD as a function of SNR for the boundary indicator functions given by Algorithm *A* and Algorithm *B*. Although the EMD functions gradually increase as the SNR decreases, the values of these functions remain reasonably small, which means that our algorithms give similar grain boundary estimates.

To quantify the statistical stability of the crystal rotation estimation, we compute the difference of the rotation estimations in noisy and noiseless cases and measure the difference of its mean and standard deviation. The mean of the difference as a function of SNR is shown in Figure 19 (middle) and the standard deviation function is shown in Figure 19 (right). Even though noise is heavy, most estimation errors are bounded by a small degree. This shows that our algorithms are statistically stable against noise.

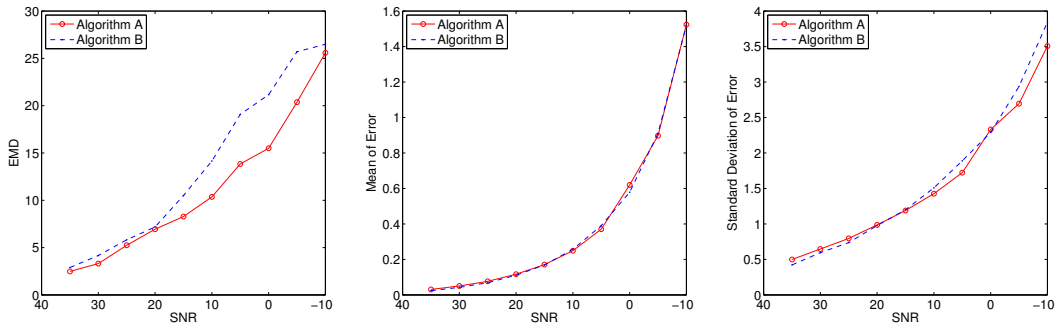


FIGURE 19. Left: The earth mover's distance (EMD) between the estimated grain boundaries of a noisy image and that of a clean image. Middle: The mean of the estimation error of crystal rotations. Right: The standard deviation of the estimation error of crystal rotations. Data plotted above is the average of 10 independent realizations.

5. CONCLUSION

This paper has proposed a new model for atomic crystal images and an efficient tool for their multiscale analysis. Through various synthetic and real data, it has been shown that the proposed methods are able to provide robust and reliable estimates of mesoscopic properties, e.g., crystal defects, rotations, elastic deformations and grain boundaries, in a short time. Since these methods are well suitable for parallelization, the runtime will be considerably reduced by parallel computing. This would be appealing in the analysis of a series of large crystal images to study the time evolution of crystals on a microscopic length scale.

Note that the recovery of local deformation gradients is not smooth and its local distortion volume is not sparsely supported in some cases, due to the estimate error of local wave vectors and the lack of regularization. This inspires future work by combining synchrosqueezed transform with regularization and optimization to find a more accurate and smoother local deformation gradient with a sparser local distortion volume.

We focus on the analysis of images with the presence of only one type of crystal and without solid and liquid interfaces in this paper. The extension is not difficult. In fact, in the presence of liquid, the solid-liquid interface can be identified as “boundary between grains” by our method. One could use imaging methods for detecting geometric objects in the cartoon part of images [6, 17] to identify the liquid part immediately after grains are identified by our method. Moreover, when the given image consists of multiple types of crystals, local Fourier transforms taken at enough sampling positions can identify reference crystals. Fixing one type of reference crystals, we apply our method to extract the boundaries, the rotations, the defects and the deformations of grains of this type. A complete analysis can be obtained by combining the results of each type of reference crystals.

Another interesting and challenging future direction is to analyze crystal images corresponding to complex lattices. First, it might be difficult to automatically identify reference crystals directly from a given image. The information hidden in the image is very redundant and hence feature extraction and dimension reduction techniques are necessary. Second, the well-separation condition for synchrosqueezed transforms may not hold due to a large number of underlying wave-like components of each grain. A 2D generalization of the 1D diffeomorphism based spectral analysis method in [33] may provide a solution to this problem.

The current methods can be easily extended to 3D crystal analysis by designing a 3D synchrosqueezed transform. This should be relevant for applications.

Acknowledgments. J.L. was partially supported by the Alfred P. Sloan foundation and National Science Foundation under award DMS-1312659. H.Y. and L.Y. were partially supported by the National Science Foundation under award DMS-0846501 and the U.S. Department of Energy’s Advanced Scientific Computing Research program under award DE-FC02-13ER26134/DE-SC0009409. H.Y. also thanks the support of National Science Foundation under award ACI-1450372 and AMS-Simons Travel Award. We are grateful to Benedikt Wirth for inspiring discussions and for providing us image data from PFC simulations. We thank Matt Elsey for helpful comments on an earlier version of the manuscript. J.L. is also grateful to Robert V. Kohn who brought his attention to this problem originally.

REFERENCES

- [1] F. F. Abraham, R. Walkup, H. Gao, M. Duchaineau, T. Diz De La Rubia, and M. Seager, *Simulating materials failure by using up to one billion atoms and the world’s fastest computer: Work-hardening*, Proc. Nat. Acad. Sci. USA **99** (2002), 5783–5787.
- [2] E. Arias-Castro, D. L. Donoho, and X. Huo, *Near-optimal detection of geometric objects by fast multiscale methods*, IEEE Trans. Inf. Theory **51** (2005), 2402–2425.
- [3] J.-F. Aujol and T. F. Chan, *Combining geometrical and textured information to perform image classification*, J. Vis. Commun. Image. R. **17** (2006), 1004–1023.
- [4] B. Berkels, A. Rätz, M. Rumpf, and A. Voigt, *Extracting grain boundaries and macroscopic deformations from images on atomic scale*, J. Sci. Comput. **35** (2008), 1–23.
- [5] M. Boerdgen, B. Berkels, M. Rumpf, and D. Cremers, *Convex relaxation for grain segmentation at atomic scale*, Vision, Modeling, and Visualization, 2010, pp. 179–186.
- [6] X. Cai, R. Chan, and T. Zeng, *A two-stage image segmentation method using a convex variant of the Mumford–Shah model and thresholding*, SIAM J. Imaging Sci. **6** (2013), 368–390.

- [7] E. J. Candès and D. L. Donoho, *Continuous curvelet transform. II. Discretization and frames*, Appl. Comput. Harmon. Anal. **19** (2005), 198–222.
- [8] T. F. Chan and L. A. Vese, *Active contours without edges*, IEEE Trans. Image Process. **10** (2001), 266–277.
- [9] I. Daubechies, J. Lu, and H.-T. Wu, *Synchrosqueezed wavelet transforms: an empirical mode decomposition-like tool*, Appl. Comp. Harmonic Anal. **30** (2011), 243–261.
- [10] I. Daubechies and S. Maes, *A nonlinear squeezing of the continuous wavelet transform based on auditory nerve models*, Wavelets in Medicine and Biology, Ed. A. Aldroubi and M. Unser, 1996, pp. 527–546.
- [11] K. R. Elder and Martin Grant, *Modeling elastic and plastic deformations in nonequilibrium processing using phase field crystals*, Phys. Rev. E **70** (2004), 051605.
- [12] M. Elsey and B. Wirth, *Segmentation of crystal defects via local analysis of crystal distortion*, Proceedings of the 8th International Conference on Computer Vision Theory and Applications (VISAPP), 2013, pp. 294–302.
- [13] ———, *A simple and efficient scheme for phase field crystal simulation*, ESAIM: Math. Mod. Num. Anal. **47** (2013), 1413–1432.
- [14] ———, *Fast automated detection of crystal distortion and crystal defects in polycrystal images*, Multi. Model. Simul. **12** (2014), 1–24.
- [15] W. A. Götz and H. J. Druckmüller, *A fast digital Radon transform – An efficient means for evaluating the Hough transform*, Pattern Recogn. **28** (1995), 1985–1992.
- [16] J. Illingworth and J. Kittler, *A survey of the Hough transform*, Comput. Vision Graph. Image Process. **44** (1988), 87–116.
- [17] M. Jung, G. Peyré, and L. Cohen, *Nonlocal active contours*, SIAM J. Imaging Sci. **5** (2012), 1022–1054.
- [18] W. E. King, G. H. Campbell, S. M. Foiles, D. Cohen, and K. M. Hanson, *Quantitative HREM observation of the $\Sigma 11(113)/[\bar{1}10]$ grain-boundary structure in aluminium and comparison with atomistic simulation*, J. Microsc. (1998), 131–143.
- [19] C. Kittel, *Introduction to solid state physics* (7th Ed.), Wiley, 1995.
- [20] Y. Meyer, *Oscillating patterns in image processing and nonlinear evolution equations: The Fifteenth Dean Jacqueline B. Lewis Memorial Lectures*, American Mathematical Society, Boston, MA, USA, 2001.
- [21] D. Mumford and J. Shah, *Optimal approximations by piecewise smooth functions and associated variational problems*, Comm. Pure Appl. Math. **42** (1989), 577–685.
- [22] O. Pele and M. Werman, *Fast and robust Earth Mover's Distances*, Computer Vision, 2009 IEEE 12th International Conference on, 2009, pp. 460–467.
- [23] B. Sandberg, T. F. Chan, and L. A. Vese, *A level-set and Gabor-based active contour algorithm for segmenting textured images*, UCLA Department of Mathematics CAM report, 2002.
- [24] H. M. Singer and I. Singer, *Analysis and visualization of multiply oriented lattice structures by a two-dimensional continuous wavelet transform*, Phys. Rev. E **74** (2006), 031103.
- [25] E. Strekalovskiy and D. Cremers, *Total variation for cyclic structures: Convex relaxation and efficient minimization*, Computer Vision and Pattern Recognition (CVPR), 2011 IEEE Conference on, 2011, pp. 1905–1911.
- [26] A. Stukowski and K. Albe, *Dislocation detection algorithm for atomistic simulations*, Model. Simul. Mater. Sci. Eng. **18** (2010), 025016.
- [27] ———, *Extracting dislocations and non-dislocation crystal defects from atomistic simulation data*, Model. Simul. Mater. Sci. Eng. **18** (2010), 085001.
- [28] M. Unser, *Texture classification and segmentation using wavelet frames*, IEEE Trans. Image Proc. **4** (1995), 1549–1560.
- [29] L. A. Vese and T. F. Chan, *A multiphase level set framework for image segmentation using the Mumford and Shah model*, Int. J. Comput. Vision **50** (2002), 271–293.
- [30] L. A. Vese and S. J. Osher, *Modeling textures with total variation minimization and oscillating patterns in image processing*, J. Sci. Comput. **19** (2003), 553–572 (English).
- [31] H.-T. Wu, *Instantaneous frequency and wave shape functions (I)*, Appl. Comp. Harmonic Anal. **35** (2013), 181–199.
- [32] H. Yang, *Robustness analysis of synchrosqueezed transforms*, arXiv:1410.5939 [math.ST] (2014). preprint.
- [33] ———, *Synchrosqueezed wave packet transforms and diffeomorphism based spectral analysis for 1D general mode decompositions*, Appl. Comput. Harmon. Anal. **39** (2015), no. 1, 33–66.
- [34] H. Yang, J. Lu, W.P. Brown, I. Daubechies, and L. Ying, *Quantitative canvas weave analysis using 2-D synchrosqueezed transforms: Application of time-frequency analysis to art investigation*, Signal Processing Magazine, IEEE **32** (2015July), no. 4, 55–63.
- [35] H. Yang and L. Ying, *Synchrosqueezed wave packet transform for 2D mode decomposition*, SIAM J. Imaging Sci. **6** (2013), 1979–2009.

- [36] ———, *Synchrosqueezed curvelet transform for two-dimensional mode decomposition*, SIAM J. Math. Anal. **46** (2014), no. 3, 2052–2083.
- [37] Z. Yu and C. Bajaj, *Detecting circular and rectangular particles based on geometric feature detection*, J. Struct. Biol. **145** (2004), 168–180.
- [38] X. Zeng, B. Gipson, Z. Y. Zheng, L. Renault, and H. Stahlberg, *Automatic lattice determination for two-dimensional crystal images*, J. Struct. Biol. **160** (2007), 353–361.

DEPARTMENT OF MATHEMATICS, DUKE UNIVERSITY

E-mail address: haizhao@math.duke.edu

DEPARTMENTS OF MATHEMATICS, PHYSICS, AND CHEMISTRY, DUKE UNIVERSITY

E-mail address: jianfeng@math.duke.edu

DEPARTMENT OF MATHEMATICS AND INSTITUTE FOR COMPUTATIONAL & MATHEMATICAL ENGINEERING, STANFORD UNIVERSITY

E-mail address: lexing@math.stanford.edu